

The synergistic role of Ni-Co bimetallic catalyst for H₂-rich syngas production via glycerol dry reforming

Mohd-Nasir Nor Shafiqah^a, Sumaiya Zainal Abidin^{b,c,*}, Nurul Asmawati Roslan^a,
Osarieme Uyi Osazuwa^b, Issara Chanakaewsomboon^d

^a Faculty of Chemical and Process Engineering Technology, Universiti Malaysia Pahang, Lebuhraya Tun Razak, 26300, Gambang, Kuantan, Pahang, Malaysia

^b Centre for Research in Advanced Fluid & Processes (FLUID CENTRE), Universiti Malaysia Pahang, 26300 Gambang, Kuantan, Pahang, Malaysia

^c Faculty of Chemical Engineering, Industrial University of Ho Chi Minh City, 12 Nguyen Van Bao St, Go Vap, Ho Chi Minh City, Viet Nam

^d Faculty of Environmental Management, Prince of Songkla University, Songkhla, Thailand

ARTICLE INFO

Keywords:

Glycerol dry reforming
Ni-Co Bimetallic
Al₂O₃
Aluminium dross
Syngas
Hydrogen

ABSTRACT

A by-product of biodiesel manufacturing, glycerol, is known for its potential to generate syngas via the glycerol dry reforming (GDR) reaction. This study evaluates monometallic and bimetallic Nickel–Cobalt (Ni–Co) (with 15%Co, 3%Ni–12%Co, 4.5%Ni–10.5%Co, 7.5%Ni–7.5%Co, 10.5%Ni–4.5%Co and 15%Ni loading) on Alumina (Al₂O₃) support extracted from aluminium dross. The catalysts were prepared using an ultrasonic-assisted impregnation process and used in GDR at temperatures ranging from 873 to 1173 K at stoichiometric feed ratio. Analyses result showed that the diluting impact of Ni–Co bimetallic precursors resulted in a reduction of metal crystallite size and improved H₂ and CO₂ uptake. The conversion of glycerol and product yield were in the order of 3%Ni–12%Co/Al₂O₃ > 4.5%Ni–10.5%Co/Al₂O₃ > 7.5%Ni–7.5%Co/Al₂O₃ > 10.5%Ni–4.5%Co/Al₂O₃ > 15%Co/Al₂O₃ > 15%Ni/Al₂O₃, with 3%Ni–12%Co/Al₂O₃ having values of 75.6%, 64.7% and 44.8%, for glycerol conversion, H₂ and CO yield respectively. All catalysts achieved product ratios ranging from 1.20 to 1.44. The high oxygen vacancies in Ni–Co bimetallic catalysts aided the reduction of carbon formation. Enhanced Ni–Co particles dispersion on Al₂O₃ support reduced the agglomeration of metal particles, thus, creating smaller crystallite size. The changes in binding energy peaks of Ni and Co were indicative of strong electronic interaction which created Ni–Co bimetallic alloys. 3%Ni–12%Co was regarded as the best catalyst for this study since it was effective in enhancing the conversion of glycerol and product yield.

1. Introduction

Fossil fuels are extensively employed to meet global energy demands. It is recorded that petroleum-based resources contribute to almost 80% of energy consumption in the world and the demand for natural gas worldwide is also expected to rise every year by 40% [1]. However, the downside effect, i.e., excess greenhouse gas emissions, global warming, air pollution, and exhaustion of crude oil resources, have prompted both the industrial and academic sectors to seek for renewables and viable eco-friendly alternatives. Therefore, future energy sources are gravitating toward syngas (H₂ and CO). The most conventional and economical process for syngas production is the methane (CH₄) reforming reaction and a lot of studies have been conducted in this regard [2]. Nevertheless, one of the setbacks from these technologies is

the utilization of natural gas, which is unsustainable. Recently, hydrocarbons like glycerol have become attractive feedstocks for production of H₂ rich syngas. Glycerol is always produced in excess during biodiesel production, thus resulting in a decrease in its market worth. If syngas can be produced from glycerol, value would be added to the process and the cost of biodiesel production will reduce [3]. Glycerol dry reforming (GDR) (as shown in Eq. (1)) is considered as an environmentally sustainable method for producing syngas since it uses both CO₂ gas (greenhouse gas) and glycerol (by-product from biodiesel production) as feedstock.



Despite these benefits, the key issues in the GDR reaction are catalyst deactivation caused by carbon deposition and active metals sintering. To

* Corresponding author. Centre for Research in Advanced Fluid & Processes (FLUID CENTRE), Universiti Malaysia Pahang, 26300 Gambang, Kuantan, Pahang, Malaysia.

E-mail address: sumaiya@ump.edu.my (S.Z. Abidin).

<https://doi.org/10.1016/j.joei.2022.09.008>

Received 11 May 2022; Received in revised form 21 September 2022; Accepted 26 September 2022

Available online 30 September 2022

1743-9671/© 2022 Energy Institute. Published by Elsevier Ltd. All rights reserved.

overcome these recurring problems, research in this field has focused on designing effective metals and supports capable of improving catalytic performance and reducing carbon deposition. The selection of support can help to improve interaction, enhance catalyst reducibility and mitigate the formation of carbon [4]. A wide variety of supports for metal active sites has been tested in reforming reactions, ranging from various acidic to basic supports. Alumina (Al_2O_3) is the most often used support in reforming reactions because it is thermally stable and possesses high surface area. More also, the strong basic property of the Al_2O_3 support enables better redox ability and storage of lattice oxygen to enhance the catalytic performance [5].

Support materials for catalysts are commercially available, however their added cost contribute to making the over cost of catalytic processes reasonably high. Waste materials employed as support now attracts attention from researchers since they are cheaper and promote a better environment. For instance, Bepari et al. investigated solid waste from thermal power plants known as fly ash as support in glycerol steam reforming. The authors reported 98.6% of glycerol conversion under the optimum conditions which was ascribed to the excellent Ni metal interaction with fly ash support [6]. Recently, Roslan et al. discovered that aluminium dross (AD) can be a waste material source of Al_2O_3 for catalytic studies [7]. The utilization of AD as catalyst support is potentially advantageous to both the academic and industrial sectors. Hence, using extracted Al_2O_3 from AD as support in reforming reactions is considered an attractive alternative which can effectively reduce the overall production cost compared to commercial Al_2O_3 .

With respect to the catalyst activity, metals play a significant role in reforming reaction by providing active sites for reaction to take place. Ni-metal has been established for reforming reactions because it is highly active towards hydrocarbon reforming and it possesses good compatibility with a wider ranger of support. Also, Ni has the ability to effectively crack C–C and C–H bonds while promoting side reactions that results in enhanced H_2 production [8]. Nonetheless, Ni-based catalysts tend to deactivate during the reforming reaction due to carbon attack on its active sites and thermal Ni sintering [9]. Thus, combining metallic catalysts (bimetallic) can contribute to modifying the catalyst's surface structure which can potentially improve performance. Literature has shown that Ni–Co bimetallic catalysts are active and can resist carbon formation effectively because of the presence of Co which has high oxygen affinity [10]. Morealso, Co-based catalysts are known to resist carbon formation by controlling the oxidation rate of carbon at the catalyst surface [11]. However, they are still prone to deactivation due to metallic Co oxidation and spinel structural formations. Studies have proposed Ni–Co bimetallic catalysts systems to minimize oxidation and sintering of metallic Co and Ni [12].

Wang et al. report suggested that when bimetallic Co–Ni catalysts is compared with its monometallic counterpart, it performed better with regards to enhanced anti-sintering and coking resistivity due to improved metal dispersion and metal-support interaction during the glycerol steam reforming reaction [13]. Another study by Wang et al. revealed the effect of transition metals/attapulgite catalyst on glycerol steam reforming. Results showed that bimetallic catalysts outperformed its mono-metallic counterparts due to enhanced catalytic properties [14]. Application of catalysts on GDR reaction mainly focused on Ni-based catalysts. Apart from that, there are also noble metals as active metals such as Pt, Pd, Ir, Ru, Rh [15,16]. Promoters such as La, Re, Ag and Ru has been reported in GDR previously [17–19]. As seen in Table S1 (supplementary data), till date, there is no study available with regard to the effect of bimetallic catalysts on GDR reaction. Thus, in the present study, the effect of bimetallic Ni–Co catalyst towards enhancing the physicochemical characteristics of the Ni–Co/ Al_2O_3 catalysts has been reported and evaluated in GDR reaction.

2. Experimental

2.1. Catalyst preparation

2.1.1. Preparation of Al_2O_3 as support

The acid leaching-precipitation process was employed to synthesize Al_2O_3 as reported by Roslan et al. [20].

2.1.2. Preparation of mono-metallic and bimetallic catalysts

The selection of total metal loading as 15% is based on the screening process which resulted in 15% as the best metal loading. 15% of metal loading was also found to be adequate for the GDR reaction to produce high product yield [18,19,21]. Monometallic 15%Ni/ Al_2O_3 and 15% Co/ Al_2O_3 was prepared using the ultrasonic-assisted impregnation technique by adding Ni or Co nitrate precursors (Merck type) into a beaker with distilled water. The solution was mixed with extracted Al_2O_3 in an ultrasonication water bath for 4 h at 353 K. The resulting sample was subsequently dried overnight and calcined in furnace at 1223 K for 5 h.

The same process was used to produce bimetallic Ni–Co/ Al_2O_3 catalysts with various bimetallic loadings; 3%Ni–12%Co, 4.5%Ni–10.5% Co, 7.5%Ni–7.5%Co, 10.5%Ni–4.5%Co and 12%Ni–3%Co. A solution of Ni and Co nitrate precursors (Merck) were mixed with 1 g of Al_2O_3 , placed in an ultrasonication water bath, and then dried in an oven overnight. The sample was further calcined in a furnace at 1223 K for 5 h. The following list summarizes the samples of Ni–Co bimetallic catalyst prepared for this work; 3%Ni–12%Co/ Al_2O_3 , 4.5%Ni–10.5%Co/ Al_2O_3 , 7.5%Ni–7.5%Co/ Al_2O_3 , 10.5%Ni–4.5%Co/ Al_2O_3 and 12%Ni–3% Co/ Al_2O_3 .

2.2. Catalyst characterization methods

The physical properties of the catalysts were analysed via N_2 -adsorption of Micromeritics ASAP-2020. The mean crystallite size and the crystalline phases of the catalysts (fresh and spent) were obtained from the X-ray Diffractogram (using the Rigaku Miniflex II technique). Patterns were recorded at $2\theta = 3^\circ\text{--}80^\circ$ (at 0.02° increment) with 1°min^{-1} scan speed. A Micromeritics AutoChem II-2920 equipment was employed to ascertain the reduction capacity of the catalyst. Using a Hydrogen temperature-programmed reduction (H_2 -TPR) step, the procedure was carried out at 373 K for 30 min in a He flow (50 ml min^{-1}) to ensure all moisture and impurities contents are eliminated. This was followed by sample reduction in a flow of 10% H_2/Ar mixture in the temperature range 373–1173 K. Subsequently, the temperature was held for 30 min at 1173 K before being allowed to cool to ambient temperature. The process was repeated with the same equipment to obtain the basicity of the catalysts sample by using CO_2 this time (CO_2 -TPD). The desorption process carried out at 1073 K at a rate of 10 K min^{-1} . Field emission scanning electron microscope (FESEM) (JEOL/JSM-7800F model) carried out at ambient temperature and between 5 and 15 kV was employed to obtain the catalysts' morphology and elemental composition. Furthermore, the catalysts' chemical composition was obtained via the energy dispersion X-ray (EDX) linked to the FESEM system. TGA Q500 unit was used to determine the carbon type deposited and its quantity using the Temperature-programmed oxidation (TPO) technique. For this process, 20% O_2/N_2 with flowrate of 100 mL min^{-1} was purged through the process as the sample was heated from 373 to 1023 K before a 30 min period of isothermal oxidation.

A ULVAC-PHI 5000 unit for carrying out X-ray photoelectron spectroscopy (XPS) was used in this study. The excitation source was Al K α with X-ray power of 300 W and an energy resolution lower than 0.65 eV. The internal composition of the catalysts samples was determined using the transmission electron microscopy (TEM). During this analysis, the samples went through an ultrasonic process for 30 min in ethanol. For each analysis, a Philips CM 12 TEM microscope was used to analyse the sample droplets after they had been placed on Cu micro-grid coated with

thin carbon film and allowed to dry for 5 min.

2.3. Procedure for glycerol dry reforming (GDR)

GDR reaction catalytic testing was conducted in a fixed bed reactor by varying the temperature (873, 973, 1073 and 1173 K) at CO₂ to glycerol ratio (CGR) of 1. Approximately 0.1 g of catalyst on quartz wool was positioned in the temperature-controlled furnace in the reactor. The feed streams to the reactor were mapped with mass flow meters to control the flowrate effectively. Catalyst reduction was carried out using 50% H₂/N₂ as reducing agent in a total stream of 50 mL min⁻¹ for 1 h. Post reduction, HPLC pump was used to inject glycerol into the reactor employing a flow motion downwards. At the outlet of the reactor, a gas wash bottle with a drierite bed was positioned to absorb all moisture content of the outlet gas. The flowrate of the product was monitored with the bubble meter while sample gas was collected in a sampling bag. 120 mL min⁻¹ and 72 L g_{cat}⁻¹ h⁻¹ were the feed gas flow rate and the gas hourly space velocity (GHSV) utilized in an 8 h reaction time. The Gas chromatography (GC) was employed to obtain the composition of the exit gas. Schematic diagram of the experimental set-up for GDR reaction was illustrated in the supplementary data (see Fig. S1). The following Eqs. (2)–(6) were used to calculate the glycerol conversion, products yield (H₂ and CO), and product ratio (H₂/CO) in the GDR reaction.

The conversion of glycerol into gaseous product:

$$X_{C_3H_8O_3}(\%) = \frac{2F_{H_2} + 4F_{CH_4}}{8F_{C_3H_8O_3}} \times 100 \quad (2)$$

Hydrogen and CO yield:

$$Y_{H_2}(\%) = \frac{2 \times F_{H_2}}{8 \times F_{C_3H_8O_3}^n} \times 100 \quad (3)$$

$$Y_{CO}(\%) = \frac{F_{CO}}{3 \times F_{C_3H_8O_3}} \times 100 \quad (4)$$

Product formation rates:

$$r_i(\text{mol g}_{\text{cat}}^{-1} \text{s}^{-1}) = \frac{y_i \times F_i^{\text{outlet}}}{W} \quad (5)$$

$i = \text{H}_2, \text{CO}, \text{CO}_2 \text{ and } \text{CH}_4$

$y_i = \text{dry basis composition of product } i$

$F_{i,\text{outlet}} = \text{molar flow rate of component } i \text{ (mol s}^{-1}\text{)}$

$W = \text{weight of catalyst (g)}$

Product ratio, H₂/CO:

$$\frac{H_2}{CO} = \frac{r_{H_2}}{r_{CO}} \quad (6)$$

3. Result and discussions

3.1. Textural properties

The physical properties of the Al₂O₃, mono- and bimetallic catalysts are shown in Table 1. BET surface area of Al₂O₃ support was 267.5 m² g⁻¹ with the value decreasing to 165.3 m² g⁻¹ and 166.4 m² g⁻¹, when Ni and Co were incorporated into Al₂O₃ support to form the catalysts. The decrease is ascribed to the dispersion of metal components on the catalysts' surface during ultrasonic impregnation. Partial pore-clogging induced by the dispersion of metal oxides into the porous Al₂O₃ support was responsible for the diffusion [22]. The investigation of N₂-physorption on the surface area of catalysts revealed minimal changes in this order; Al₂O₃ > 15%Co/Al₂O₃ > 15%Ni/Al₂O₃ > 3%Ni-12%Co/Al₂O₃ > 4.5%Ni-10.5%Co/Al₂O₃ > 7.5%Ni-7.5%Co/Al₂O₃ > 10.5%Ni-4.5%Co/Al₂O₃ > 12%Ni-3%Co/Al₂O₃.

The incorporation of mono-metallic Ni and Co into Al₂O₃ support

Table 1

Textural properties of mono- and Ni-Co bimetallic catalysts.

Catalyst	BET surface area (m ² g ⁻¹)	Average pore volume (cm ³ g ⁻¹) ^a	Average pore diameter (nm) ^b	Average metal particles size (nm) ^c
Al ₂ O ₃	267.5	0.85	16.2	–
15%Ni/Al ₂ O ₃	165.3	0.64	18.3	12.63
15%Co/Al ₂ O ₃	166.4	0.67	18.0	12.55
3%Ni-12%Co/Al ₂ O ₃	163.4	0.61	17.0	9.25
4.5%Ni-10.5%Co/Al ₂ O ₃	161.3	0.60	16.7	9.68
7.5%Ni-7.5%Co/Al ₂ O ₃	159.1	0.58	16.4	10.32
10.5%Ni-4.5%Co/Al ₂ O ₃	158.7	0.55	16.1	11.16
12%Ni-3%Co/Al ₂ O ₃	155.0	0.51	16.0	11.45

^a obtained at p/p⁰ equivalent to 0.99.

^b From Barret-Joyner-Halenda desorption method.

^c estimated with Scherrer model at the highest intensity values for NiO (37.26°), Co₃O₄ (36.88°) and NiCo₂O₄ (35.58°).

slightly enlarged the pore diameter because of the agglomeration and subsequent expansion of Ni and Co metals, respectively. In contrast, the pore diameter reduced with the introduction of the bi-metals suggesting a well dispersion of the bi-metals in the catalyst support. According to IUPAC classification, the physisorption isotherm for all examined catalysts exhibited mesoporous type IV isotherm. In the multilayer adsorption of the mesoporous structure, the IV mesoporous isotherm was evident indicative of the presence of hysteresis loop. The catalysts classification was H1 hysteresis loop ascribed to narrow pore size distribution of the catalysts [23,24].

3.2. X-ray diffraction (XRD)

XRD analyses of Al₂O₃, Co/Al₂O₃, Ni/Al₂O₃, and Ni-Co/Al₂O₃ at various loadings are shown in Fig. 1. For each sample, XRD peaks for γ-Al₂O₃ were detected at 32.62°, 37.51°, 39.50°, 42.63°, 45.75° and 67.12° (JCPDS: 04–0858). For the Co/Al₂O₃ catalyst, the representative peaks for Co₃O₄ were detected at 31.76°, 36.88°, 45.55°, and 55.51° (JCPDS: 74–2120). The peaks for CoAl₂O₄ spinel (JCPDS: 82–2246) was also visible in the Co/Al₂O₃ catalyst at 59.25° and 65.13°. This peak can be attributed to the strong interaction between Co and Al₂O₃ support [25]. Meanwhile, NiO (JCPDS: 78–0643) peaks were discovered at 37.26°, 43.26° and 62.88° for the Ni/Al₂O₃ catalyst. The peaks assigned for spinel NiAl₂O₄ phase (JCPDS: 10–0339) were presented at 37.26° and 75.38°. The spinel phase of CoAl₂O₄ and NiAl₂O₄ were formed at high calcination temperature as a result of intense interaction between metal and support (see Eqs. (7) and (8)) [26].



Fig. 1(d)–(h) illustrates XRD patterns for Ni-Co/Al₂O₃ at various metal loadings. The diffraction line for Al₂O₃, Co₃O₄, CoAl₂O₄, NiO and NiAl₂O₄ were visible in all bimetallic catalysts. The peaks' intensity for Co₃O₄ and CoAl₂O₄ increased consistently with the amount of Co present in each Ni-Co catalyst. Similar trend was observed for the peaks of NiO and NiAl₂O₄. The spinel composite crystalline oxide (NiCo₂O₄) (JCPDS:20–0781) peaks were formed for the Ni-Co/Al₂O₃ catalysts during the calcination step at 31.13°, 35.58°, 43.26°, 48.61° and 65.17° as shown in Eq. (9) [26,27].

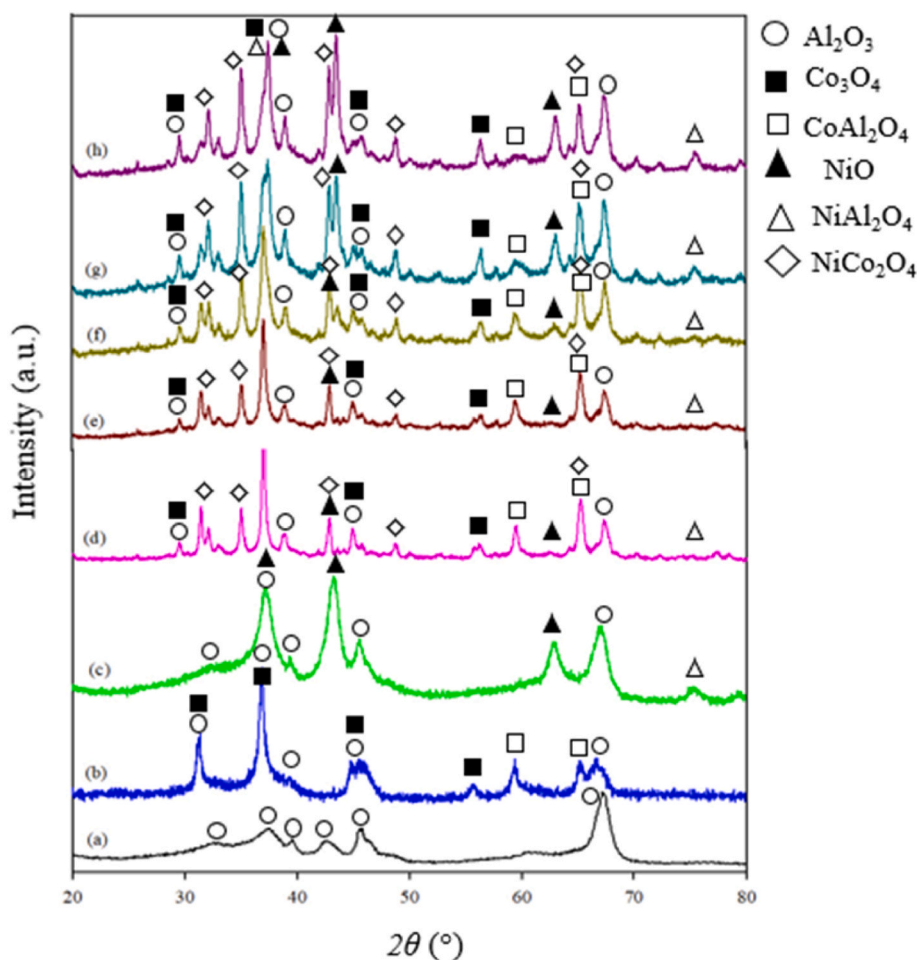


Fig. 1. XRD for fresh catalysts including (a) Al_2O_3 , (b) 15%Co/ Al_2O_3 , (c) 15%Ni/ Al_2O_3 (d) 3%Ni-12%Co/ Al_2O_3 , (e) 4.5%Ni-10.5%Co/ Al_2O_3 , (f) 7.5%Ni-7.5%Co/ Al_2O_3 , (g) 10.5%Ni-4.5%Co/ Al_2O_3 and (h) 12%Ni-3%Co/ Al_2O_3 .



The average metal particle sizes of the mono- and bimetallic Ni-Co catalysts are tabulated in Table 1. The Scherrer model gave the average crystallite size (d_m) calculated by employing the most intense metal peak (NiO (37.26°), Co_3O_4 (36.88°) and NiCo_2O_4 (35.58°)) (Eq. (10)).

$$d_m(\text{nm}) = \frac{0.94\lambda}{\beta \cos \theta} \quad (10)$$

λ , β , θ , represents wavelength, line broadening at half maximum intensity and, Bragg angle, respectively.

The changes in the average metal particle sizes for each catalyst follows the trend; 15%Ni/ Al_2O_3 (12.63 nm) > 15%Co/ Al_2O_3 (12.55 nm) > 12%Ni-3%Co/ Al_2O_3 (11.45 nm) > 10.5%Ni-4.5%Co/ Al_2O_3 (11.16 nm) > 7.5%Ni-7.5%Co/ Al_2O_3 (10.32 nm) > 4.5%Ni-10.5%Co/ Al_2O_3 (9.68 nm) > 3%Ni-12%Co/ Al_2O_3 (9.25 nm). The bimetallic catalysts have smaller average crystallite size compared to the mono-metallic catalysts due to the diluting effect of bimetallic precursors that prevent Ni and Co particles from agglomerating. The reduction in crystallite size confirms that the Ni-Co bimetallic alloys was formed due to the solid phase reaction of Ni and Co oxides [27]. With an average metal particle size of 9.25 nm, 3%Ni-12%Co/ Al_2O_3 had the smallest average metal particle size of all the catalyst loadings, indicative of higher metal dispersion. Increased cobalt content in the bimetallic Ni-Co reduces the intensity of the NiCo_2O_4 peaks, resulting in increased dilution of both metals and simultaneously improvement in the metal dispersion. This observation is supported by reduction in the crystallite size of the 12%Ni-3%Co/ Al_2O_3 catalyst from 11.45 nm to 9.25 nm of the

3%Ni-12%Co/ Al_2O_3 catalyst, showing better metal dispersion when Co content was higher in the catalysts. The higher amount of Co metal in Ni-Co bimetallic catalysts results in smaller crystallite size which is in line with studies by Dachenko et al. This phenomenon was due to the gradual replacement of Ni atoms by Co atoms in the crystal lattice, resulting in the formation of solid solutions [28].

3.3. H_2 - temperature programmed reduction (H_2 -TPR)

Fig. 2 illustrates the H_2 -TPR profiles for all catalysts in this study. Fig. 2(a) shows three characteristics peaks for the Co/ Al_2O_3 catalyst. The first peak at 633.3 K represents the two-step reduction of Co_3O_4 (see Eq. (11) and Eq. (12)) while the peak located around 793.5 K is ascribed to the reduction of Co particles, that were evenly dispersed on the Al_2O_3 support [29]. Additionally, the peak detected at temperature beyond 850 K is linked to the reduction of the spinel structure of CoAl_2O_4 during the dispersion of Co on the Al_2O_3 support [25]. TPR peaks for the Ni/ Al_2O_3 (Fig. 2(b)) was linked to the metal oxides and spinel metal oxides reduction. In the first reduction peak, the reduction of NiO to metallic Ni (refer to Eq. (13)) revealed weak metal and support interaction. The second peak at 974.2 K is assigned to reduction of well dispersed NiO which had stronger interaction with the support [30].



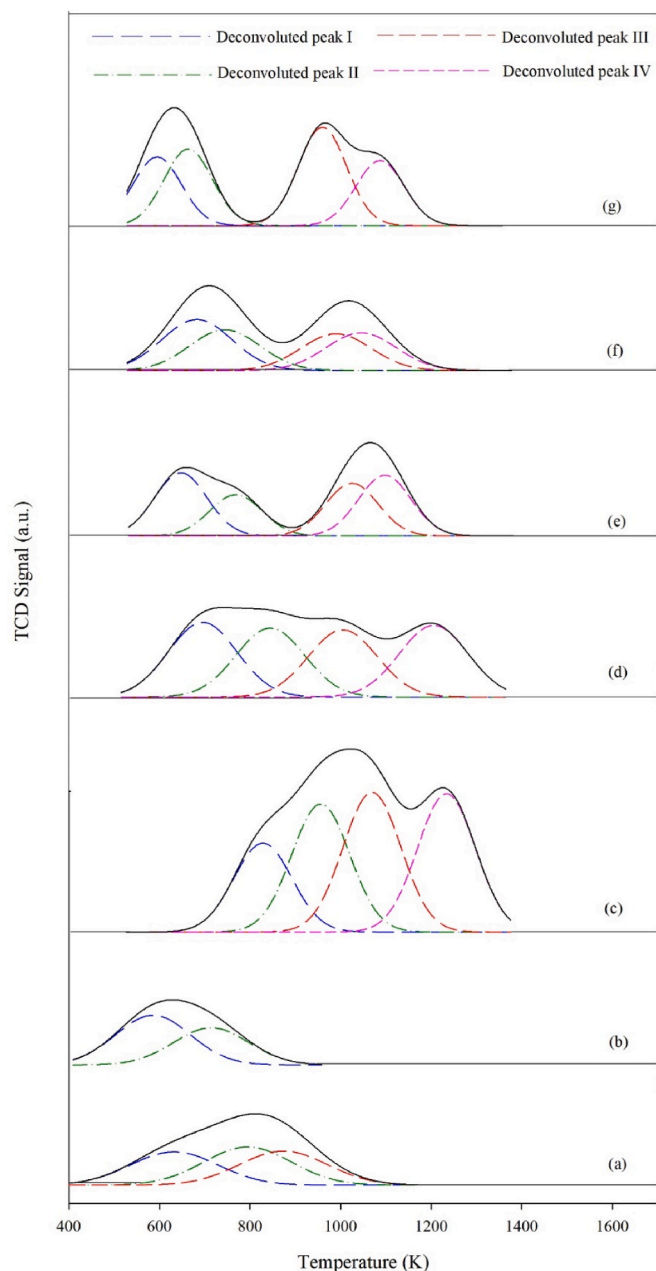


Fig. 2. H₂-TPR analyses of (a) 15%Co/Al₂O₃, (b) 15%Ni/Al₂O₃, (c) 3%Ni–12%Co/Al₂O₃, (d) 4.5%Ni–10.5%Co/Al₂O₃, (e) 7.5%Ni–7.5%Co/Al₂O₃, (f) 10.5%Ni–4.5%Co/Al₂O₃ and (g) 12%Ni–3%Co/Al₂O₃.

For the Ni–Co bimetallic catalysts, four distinctive peaks were seen. Peak I and peak II ranging from 300 to 800 K were attributed to the reduction of single metal oxides such as NiO and Co₃O₄. Meanwhile, peaks III and IV detected at higher temperature (>800 K) were ascribed to the reduction of the spinel phase of bimetallic samples, CoAl₂O₄, NiAl₂O₄ and NiCo₂O₄, which are all consistent with the XRD analysis.

Literature shows that the particle size coupled with the degree of interaction influence the reduction temperature of metal oxides [31,32]. All the bimetallic catalysts possessed metal phases having their most obvious peak at high temperatures with the trend identified as Co content increases. 3%Ni–12%Co/Al₂O₃ with the highest Co loading recorded higher reduction temperature in relation to the other catalysts because of its smaller crystallite size and this enhanced the interaction between the metal and the support [33]. Moreover, these reduction profiles suggest the formation of bimetallic phases in the catalysts. This

is because the low reduction temperature in the Ni–Co/Al₂O₃ is obvious in peak I and II which corresponds to Co₃O₄ and NiO reduction, respectively. The reduction in the bimetallic Ni–Co/Al₂O₃ catalysts promoted the metal oxides to form Ni–Co alloy [34,35]. The shift in the reduction profiles indicative of the formation of Ni–Co bimetallic alloys was also observed in previous studies [33–36].

In addition, the amount of H₂ consumption for each catalyst was summarized in Table 2. The changes in the H₂ consumption (mmol H₂ g_{cat}⁻¹) increased in the order 15%Ni/Al₂O₃ (128.8) < 15%Co/Al₂O₃ (132.5.5) < 12%Ni–3%Co/Al₂O₃ (153.2) < 10.5%Ni–4.5%Co/Al₂O₃ (178.4) < 7.5%Ni–7.5%Co/Al₂O₃ (183.6) < 4.5%Ni–10.5%Co/Al₂O₃ (226.1) < 3%Ni–12%Co/Al₂O₃ (245.7). The bimetallic catalysts exhibited higher H₂ consumption compared to mono-metallic catalysts due to the incorporation of Co into the Ni-metal catalyst thereby enhancing the dispersion of the Ni derivatives. This phenomenon is linked to the decrease in the reduction temperature. The increase in dispersion of Ni with addition of second metal Co can be credited to the impact of dilution from Ni–Co alloy that prevents both metals particles from agglomerating. This situation leads to a greater reducible surface, most likely because of higher dispersion of the metallic phase and smaller particles size. Also, it increases the H₂ adsorption into the catalyst surface [37]. The rise in H₂ uptake in the bimetallic catalysts was indicative of improved degree of reduction of the active metal oxide.

3.4. CO₂ temperature-programmed desorption (CO₂-TPD)

The catalysts basic strength was evaluated by CO₂-TPD analysis. In general, the desorption temperature and CO₂ desorption peaks can be used to determine the basic strength of the catalysts [38]. Fig. 3 illustrates the CO₂-TPD profile for mono- and bimetallic catalysts, while data for the total basicity is tabulated in Table 3. Basic sites at <523 K represents weak sites, while, between 523 and 900 K and >900 K corresponds to medium and strong basic sites, respectively [39]. All the catalyst exhibits peaks for basic sites, most notably in the weak and medium regions. Surface hydroxyl and its species in the Al₂O₃ support are responsible for this behaviour [39]. The presence of desorption peaks at <523 K is attributed to the basic sites with low strength for the removal of adsorbed moisture, with the Ni–Co/Al₂O₃ catalysts possessing higher intensity of these peaks. In the region with medium sites, several peaks appear in Ni/Al₂O₃ and Co/Al₂O₃ catalysts while peaks with high intensity appears in the bimetallic samples. For the strong sites which represents low coordinates adsorption of O⁻ sites, Ni/Al₂O₃ exhibits a wide peak in this region [38]. Regardless, the CO₂-TPD desorption curve of 3%Ni–12%Co/Al₂O₃ exhibited three well-resolved desorption peaks centred at 363 K, 779 K and 1037 K for weak, medium, and strong sites, respectively.

The amount of CO₂ desorbed from the catalysts' surfaces during

Table 2

H₂ consumption and reduction peak temperature.

Catalyst	Reduction temperature of reduction (K)				H ₂ consumption (mmol H ₂ g _{cat} ⁻¹)
	I	II	III	IV	
15%Co/Al ₂ O ₃	619.3	786.5	872.7	–	112.4
15%Ni/Al ₂ O ₃	578.7	719.2	–	–	91.2
3%Ni–12%Co/Al ₂ O ₃	831.3	948.7	1061.2	1228.8	245.7
4.5%Ni–10.5%Co/Al ₂ O ₃	712.2	855.9	1022.6	1207.4	226.1
7.5%Ni–7.5%Co/Al ₂ O ₃	639.9	760.6	1013.1	1092.5	183.6
10.5%Ni–4.5%Co/Al ₂ O ₃	673.6	740.5	976.8	1042.6	178.4
12%Ni–3%Co/Al ₂ O ₃	390.4	696.1	970.3	1068.4	153.2

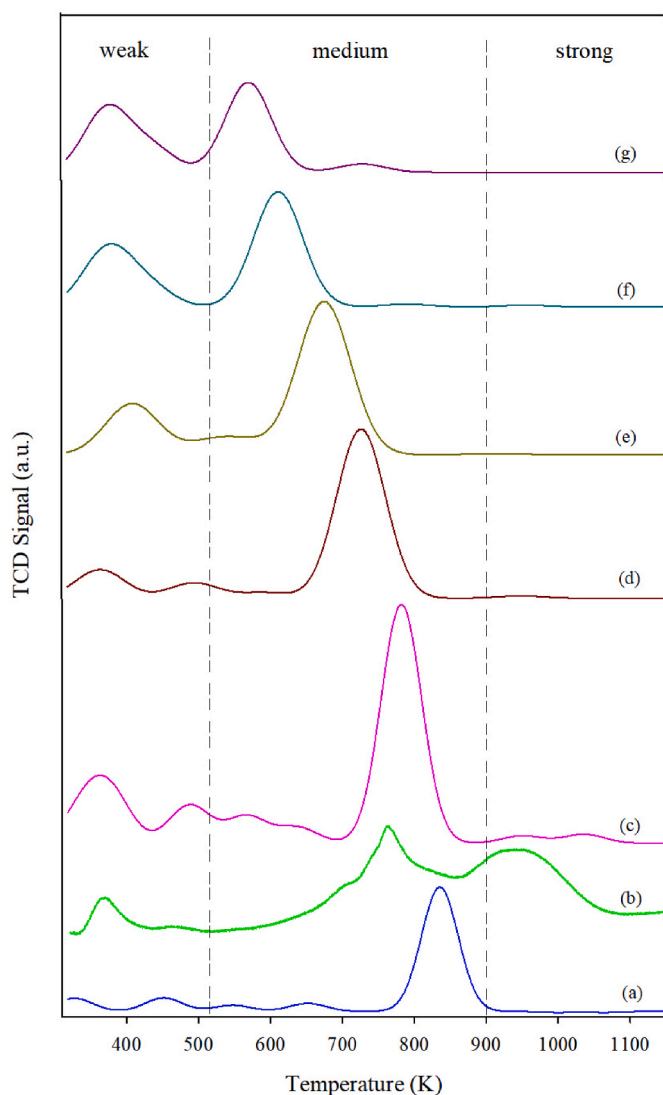


Fig. 3. CO₂-TPD for fresh catalysts (a) 15%Co/Al₂O₃, (b) 15%Ni/Al₂O₃, (c) 3% Ni–12%Co/Al₂O₃, (d) 4.5%Ni–10.5%Co/Al₂O₃, (e) 7.5%Ni–7.5%Co/Al₂O₃, (f) 10.5%Ni–4.5%Co/Al₂O₃ and (g) 12%Ni–3%Co/Al₂O₃.

Table 3

The amount of CO₂ uptake for each catalyst based on CO₂-TPD analyses.

Catalyst	CO ₂ uptake (mmol CO ₂ g _{cat} ⁻¹)			Total
	Peak I (weak site)	Peak II (medium site)	Peak III (strong site)	
15%Co/Al ₂ O ₃	63.6	123.6	15.1	202.3
15%Ni/Al ₂ O ₃	53.2	68.4	78.0	199.6
3%Ni–12%Co/Al ₂ O ₃	102.5	215.4	32.6	350.5
4.5%Ni–10.5%Co/Al ₂ O ₃	78.2	194.5	21.4	294.1
7.5%Ni–7.5%Co/Al ₂ O ₃	82.3	182.2	20.3	284.8
10.5%Ni–4.5%Co/Al ₂ O ₃	80.4	150.3	18.7	249.4
12%Ni–3%Co/Al ₂ O ₃	81.7	144.7	17.5	243.9

analysis is summarized in Table 3. Ni–Co bimetallic catalysts achieved higher CO₂ desorption compared to Ni/Al₂O₃ and Co/Al₂O₃ catalysts. Study by Turap et al. which agreed with the present analysis also reported high basicity for Ni–Co bimetallic catalysts compared to its

mono-metallic counterpart suggesting that the introduction of Co improved the catalytic properties [40]. In addition, the trend for CO₂ uptake is also similar with H₂ uptake during H₂-TPR analysis. It was further confirmed that catalysts with smaller crystallite size have higher metal-support interaction thereby possessing the ability to absorb more CO₂ during TPD analysis. There is a direct relationship between adsorbed CO₂ and the suppression of carbon formulated in-situ reaction. As a result, it potentially inhibits the occurrence of catalyst deactivation resulting in high catalytic performance with less coke formed [6].

3.5. Field emission scanning microscopy-energy dispersive X-ray (FESEM-EDX)

Fig. 4 illustrates FESEM-EDX images and elemental mapping composition of fresh 15%Co/Al₂O₃, 3%Ni–12%Co/Al₂O₃, 7.5%Ni–7.5%Co/Al₂O₃ and 10.5%Ni–4.5%Co/Al₂O₃ catalysts which was carried out to determine the distribution of metal and their composition on the catalysts surface. Based on FESEM images, the metals were scattered uniformly over the catalyst showing random distribution of the atom with the Ni–Co bimetallic catalysts showing better homogeneity than the mono-metallic Co/Al₂O₃. The bimetallic structure of Ni–Co helps to reduce the agglomerative effect of Ni and hence, produce highly dispersed metals on the support surface [41]. Furthermore, 3%Ni–12%Co/Al₂O₃ shows a highly homogeneous and well-dispersed Ni–Co on the Al₂O₃ support leading to the reduction of the crystallite size and strengthening of the metal-support interaction. The EDX mapping for each element of Co/Al₂O₃ and different Ni–Co loading further confirms reduced agglomeration for the bimetallic catalysts. Also, the introduction of Co into Ni metal reduces the sintering impact and further enhances Ni dilution into the support. This observation is evident in the 3% Ni–12%Co/Al₂O₃ catalyst which contained the highest amount of Co, hence, creating the best synergistic Ni–Co bimetallic effect.

Table 4 summarizes the elemental composition and Fig. 5 illustrates the EDX spectrum for the fresh 15%Co/Al₂O₃, 3%Ni–12%Co/Al₂O₃, 7.5%Ni–7.5%Co/Al₂O₃ and 10.5%Ni–4.5%Co/Al₂O₃ catalysts. Based on the elemental composition in Table 4, the Ni and Co metal weight percent were similar to the theoretically prepared catalysts. For example, 15%Co/Al₂O₃ contained around 15.14% of Co, 3%Ni–12%Co/Al₂O₃ with 2.97% of Ni and 12.05% of Co. Similar amount of Ni and Co were also discovered for 7.5%Ni–7.5%Co/Al₂O₃ and 10.5%Ni–4.5%Co/Al₂O₃, respectively. In addition, oxygen (O) element marked the highest composition followed by aluminium (Al) atom which were approximately within 2:3 ratio, confirming the configuration of alumina, Al₂O₃. Also, the percentage of O elemental component for each catalyst are summarized in Table 4.

3.6. Catalytic evaluation in the GDR reaction

The influence of temperature on the GDR reaction was determined at temperature ranged 873 K–1173 K and reactants ratio, $F_{CO_2} : F_{C_3H_8O_3} = 1 : 1$. As illustrated in Fig. 6(a), glycerol conversion increased significantly with increasing temperature due to the endothermicity of the GDR [42,43]. For all catalysts, the highest glycerol conversion occurred at 1073 K and drops slightly at 1173 K. This behaviour is in agreement with several findings from previous GDR studies [19,20,42]. The sequence of conversions (glycerol) followed the order; 3%Ni–12%Co/Al₂O₃ > 4.5%Ni–10.5%Co/Al₂O₃ > 7.5%Ni–7.5%Co/Al₂O₃ > 10.5%Ni–4.5%Co/Al₂O₃ > 15%Co/Al₂O₃ > 15%Ni/Al₂O₃ and remained unchanged for all reaction temperature. It is notable that bimetallic catalysts have higher glycerol conversion than their mono-metallic counterpart. This trend can be likened to the sequence of H₂ uptake in the TPR analysis (see Table 2). Therefore, increasing H₂ uptake and quantity of active metallic sites of Ni and Co could result in higher reactant conversions. Wang et al. reported similar findings in glycerol steam reforming over Ni/ATP and several other combinations of bimetallic catalyst. The authors explained that bimetallic catalysts convert

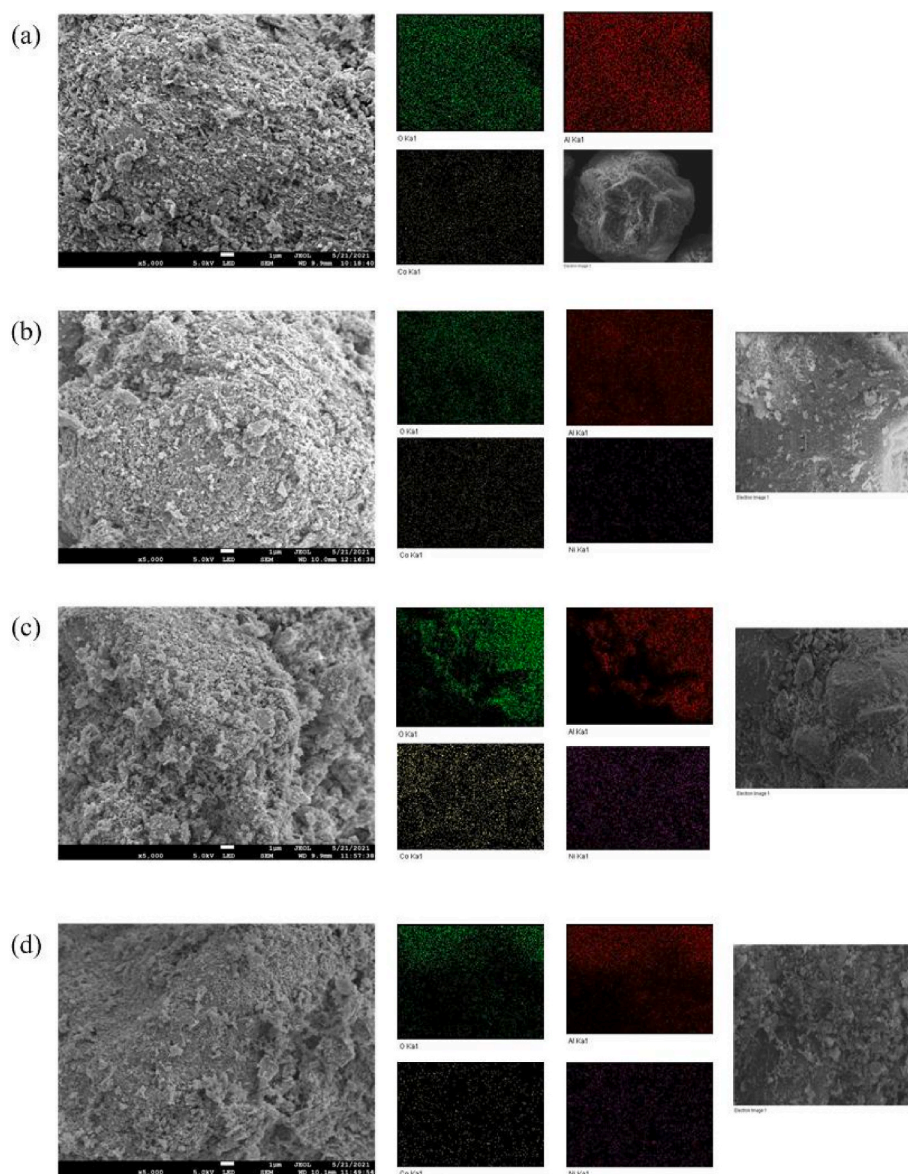


Fig. 4. FESEM-EDX images and compositional element mapping of fresh catalysts (a) 15%Co/Al₂O₃, (b) 3%Ni–12%Co/Al₂O₃, (c) 7.5%Ni–7.5%Co/Al₂O₃ and (d) 10.5%Ni–4.5%Co/Al₂O₃.

Table 4
Elemental composition from EDX analysis.

Catalyst	Elements weight (%)			
	Ni	Co	Al	O
15%Co/Al ₂ O ₃	–	15.14	32.23	52.63
3%Ni–12%Co/Al ₂ O ₃	2.97	12.05	30.45	54.53
7.5%Ni–7.5%Co/Al ₂ O ₃	7.52	7.60	31.71	53.17
10.5%Ni–4.5%Co/Al ₂ O ₃	10.53	4.45	31.88	53.14

more glycerol than single Ni/ATP due to their high reducibility [14]. More also, the increased basicity of the bimetallic catalysts contributed to improved catalytic activity, because the higher CO₂ uptake facilitated gasification of the carbonaceous species on the catalysts' surface. For all temperatures studied, 3%Ni–12%Co/Al₂O₃ bimetallic catalyst exhibited the highest glycerol conversion. Glycerol conversion improved from 65.9% to 75.6% with temperature increment from 873 to 1073 K and reduced to 72.5% at 1173 K. Furthermore, this result is also in agreement with the reducibility and basicity studies carried out where the 3%

Ni–12%Co bimetallic catalyst had the highest respective values, hence, confirming the effect of catalyst reduction and improvement of its basic site as a means to enhance the GDR activity.

Fig. 6(b) and (c) describes the temperature effects on the product yield (H₂ and CO), respectively, at temperature from 873 to 1173 K. The trend for products yield is similar to glycerol conversion where, H₂ and CO yield increased substantially with increasing temperature within 873–1073 K and decline at 1173 K. Comparative analysis between catalysts shows that all product yields followed the same trend as reactant conversion in the order; 3%Ni–12%Co/Al₂O₃ > 4.5%Ni–10.5%Co/Al₂O₃ > 7.5%Ni–7.5%Co/Al₂O₃ > 10.5%Ni–4.5%Co/Al₂O₃ > 12%Ni–3%Co/Al₂O₃ > 15%Co/Al₂O₃ > 15%Ni/Al₂O₃. Also, 3%Ni–12%Co/Al₂O₃ recorded the highest H₂ and Co yield at 1073 K with values of 64.7% and 44.8%, respectively. The increasing amount of glycerol conversion resulted in the improving H₂ and CO yields, which occurred as a result of the decomposition of glycerol at high reaction temperatures (Eq. (14)) [3]. However, recent study on GDR by Bulutoglu et al. suggested that the H₂ and CO yields were enhanced from the decomposition of glycerol and the methane dry reforming side reaction (Eq. (15)) [15].

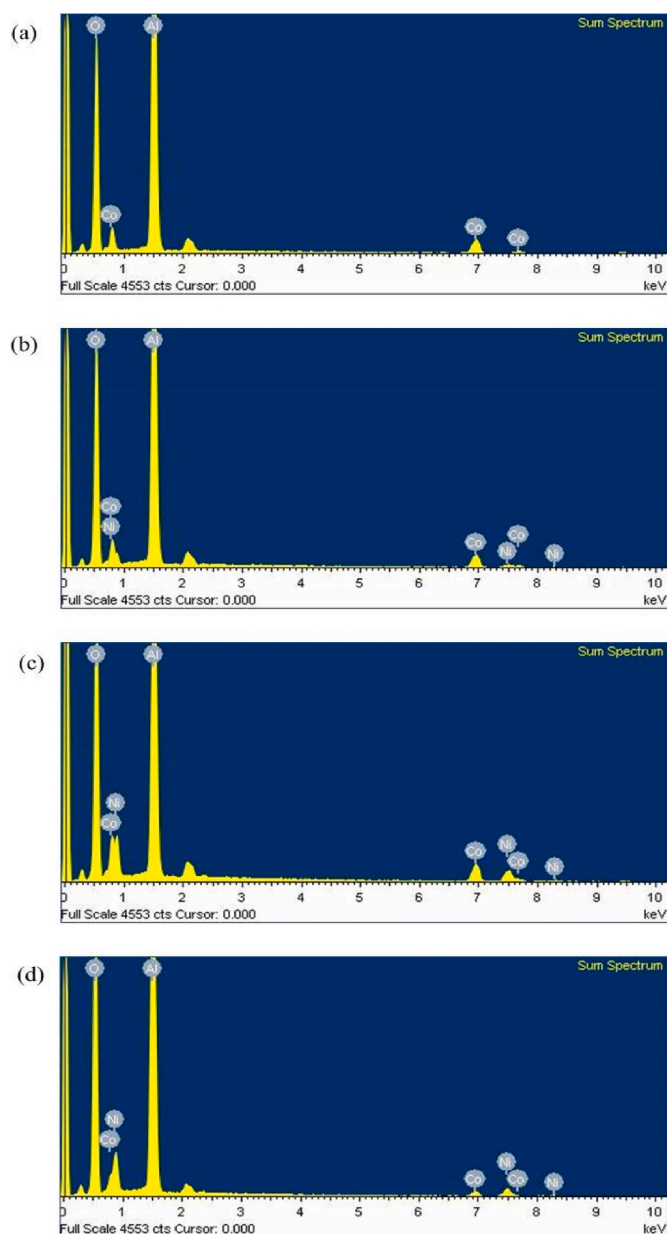


Fig. 5. EDX spectrum of (a) 15%Co/Al₂O₃, (b) 3%Ni–12%Co/Al₂O₃, (c) 7.5%Ni–7.5%Co/Al₂O₃ and (d) 10.5%Ni–4.5%Co/Al₂O₃.

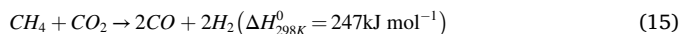


Fig. 6(d) represents the effect of temperature on the H₂/CO ratio for each catalyst where the ratio increased from 873 to 1073 K and decline at 1173 K. The trend for H₂/CO ratio is also consistent with the findings from glycerol conversion and H₂ yield, in which the ratio starts to drop beyond 1173 K. Furthermore, the findings reveal that the increase in temperature enhances the rate of the water-gas-shift reaction [21]. The obtained value H₂/CO ratio was in the range of 1.20–1.44, depending on the catalyst and the reaction temperature utilized. The process yields a favorable H₂/CO ratio for downstream generation of hydrocarbons useful as feedstock for the Fischer-Tropsch synthesis [44].

The apparent activation energy derived from the Arrhenius plot is widely used in reforming processes to justify the reactivity of catalysts without applying associated kinetic models [32]. From Fig. 7, the rate of glycerol consumption against reciprocal of reaction temperature shows

a linear relationship with correlation coefficient (R^2) around 0.97 to 0.99 (Table 5). The amount of apparent activation energy was summarized as follows; 15%Ni/Al₂O₃ (69.35 kJ mol⁻¹) > 15%Co/Al₂O₃ (68.25 kJ mol⁻¹) > 12%Ni–3%Co/Al₂O₃ (62.26 kJ mol⁻¹) > 10.5%Ni–4.5%Co/Al₂O₃ (61.31 kJ mol⁻¹) > 7.5%Ni–7.5%Co/Al₂O₃ (58.46 kJ mol⁻¹) > 4.5%Ni–10.5%Co/Al₂O₃ (55.77 kJ mol⁻¹) > 3%Ni–12%Co/Al₂O₃ (54.41 kJ mol⁻¹). Notably, the order of E_a for glycerol consumption is parallel to the trend of glycerol conversion (see Fig. 6(a)). The catalytic improvement in Ni–Co bimetallic catalysts further explained this observation.

For further verification of the Ni–Co bimetallic catalyst activity in this current research, the catalytic performance was compared with transitional and noble promoted catalysts recently reported in literature. From Table 6, bimetallic 3%Ni–12%Co/Al₂O₃ recorded higher glycerol conversion and H₂ yield at the same operating condition with promoted 5%Re–15%Ni/CaO [18] and 3%Re–15%Ni/SBA-15 [45]. More also, Ni–Co bimetallic catalyst from this work achieved higher conversion compared to noble metal promoted catalyst 3%Ag–15%Ni/Al₂O₃ using the same operating parameters [19]. Notably, GDR reaction from previous literature was conducted with lower GHSV 36 L g_{cat}⁻¹ h⁻¹, in contrast to this current work with 72 L g_{cat}⁻¹ h⁻¹. Thus, 3%Ni–12%Co/Al₂O₃ could be regarded as a promising catalyst and exhibited a comparable performance with noble metal catalysts.

3.7. Evaluation on spent catalysts

3.7.1. X-ray diffraction (XRD)

Spent catalysts analysis (XRD) was conducted post-reaction (at T = 1023 K and $F_{CO_2} : F_{C_3H_8O_3} = 1 : 1$) to ascertain the catalysts' phase stability. From the XRD results presented in Fig. 8, the presence of a tiny peak at $2\theta = 26.38^\circ$ is indicative of graphitic carbon (JCPDS: 75–0444) [25]. With respect to the intensity of the graphite peak, the amount of carbon formed in the bimetallic catalysts is less than its mono-metallic counterpart. 3%Ni–12%Co/Al₂O₃ had the smallest graphite carbon peak compared to other catalysts. Meanwhile, the graphitic carbon formation on the spent catalysts cannot be totally eliminated because of high-temperature glycerol cracking. For the spent Co-metal catalysts, peaks at 36.88° and 45.55° were detected representing the Co₃O₄ phases (JCPDS: 74–2120). This phase is linked to the re-oxidation of Co⁰ during the dry reforming reaction [46], whereas for the Ni-metal catalysts, representative peaks of Ni⁰ (JCPDS: 87–0712) occurs at 44.76° , 51.97° and 76.49° , respectively, which is associated with complete formation of Ni⁰ phase from reduction of NiO during the H₂ reduction process [47]. For Ni–Co bimetallic catalyst, the Ni⁰ phase peaks were detected in consistency with Ni/Al₂O₃ catalysts.

In contrast to Co/Al₂O₃, the Ni–Co bimetallic catalysts have three peaks at 42.75° , 48.61° and 56.14° corresponding to Co⁰ phase, which suggests that Co₃O₄ phase was completely reduced to Co⁰. Interestingly, the Co⁰ retained its active phase throughout the reaction, even under oxidizing conditions, owing to the synergistic Ni–Co metal interaction. The incorporation of Co into Ni helps to enhance the reduction of Ni into its active metallic state [41]. The NiCo₂O₄ peaks in the spent catalysts of Ni–Co bimetallic samples gradually repositioned towards higher angles (33.01° , 36.75° , 44.76° , 48.61° and 67.73°), suggesting that Ni–Co alloy was formed during the process [27].

3.7.2. X-ray photoelectron spectroscopy (XPS)

Fig. 9(a) represents the XPS of the spent 15%Co, 15%Ni, 3%Ni–12%Co, 7.5%Ni–7.5%Co and 10.5%Ni–4.5%Co catalysts, while Table 7 summarizes the binding energies for all XPS peaks in order to determine oxidation state and surface atomic composition of the catalysts. According to XPS analysis of the spent catalysts, Ni, Co, Al, C and O elements were present in the catalysts. In addition, the presence of Al 2p was detected between binding energy (BE) of 77.5 eV and 78.6 eV, which confirmed the presence of the Al₂O₃ support [48].

Fig. 9(b) shows the Co 2p spectra for selected spent catalysts with

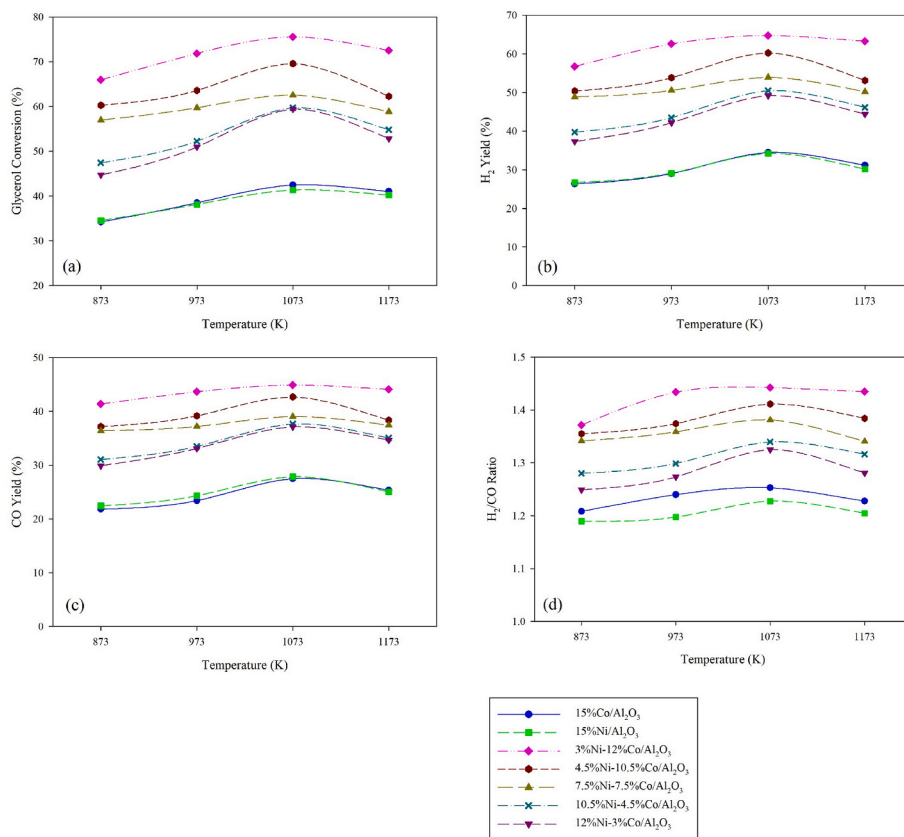


Fig. 6. Temperature effects on (a) glycerol conversion, (b) H₂ yield (c) CO yield and (d) H₂/CO ratio at 1:1.

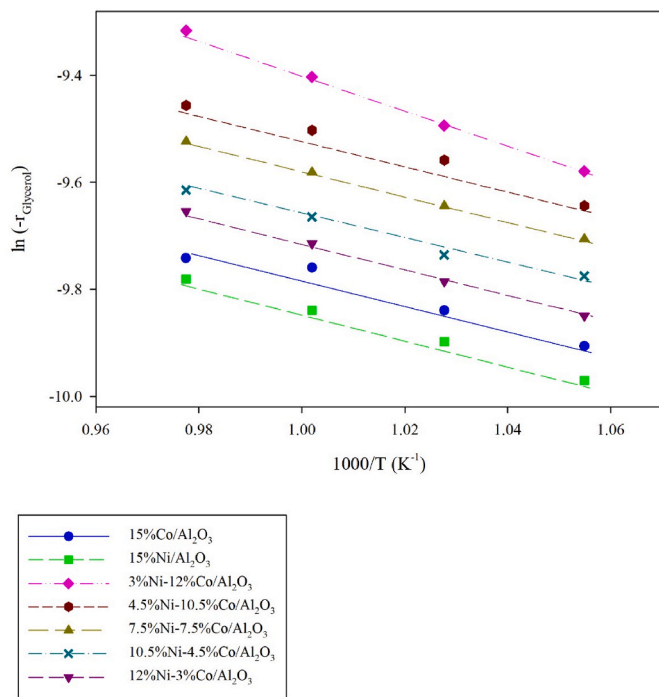


Fig. 7. Arrhenius plots for estimating apparent glycerol activation energy of all catalysts.

Gaussian deconvolution. There are three notable peaks for the Co 2p_{3/2} region at BE between 780.5 and 795.3 eV for 15%Co/Al₂O₃, 3%Ni–12%Co, 7.5%Ni-7.5%Co and 10.5%Ni-4.5%Co catalysts. These peaks

Table 5
Summary of apparent activation energy for glycerol conversion for GDR reaction.

Catalyst	Pre-exponential factor, A (s ⁻¹)	Apparent activation energy, E _a (kJ mol ⁻¹)	R ²
15%Ni/Al ₂ O ₃	0.046	69.35	0.97
15%Co/Al ₂ O ₃	0.031	68.25	0.97
3%Ni–12%Co/Al ₂ O ₃	0.022	54.41	0.99
4.5%Ni-10.5%Co/Al ₂ O ₃	0.048	55.77	0.98
7.5%Ni-7.5%Co/Al ₂ O ₃	0.028	58.46	0.99
10.5%Ni-4.5%Co/Al ₂ O ₃	0.037	61.31	0.99
12%Ni–3%Co/Al ₂ O ₃	0.025	62.26	0.98

represent Co₃O₄ and a shake-up satellite for Co 2p_{3/2} [34]. On the other hand, a similar number of peaks is seen under the Co 2p_{1/2} within the range of 792.3 eV and 808.6 eV belonging to metallic Co⁰ and satellite for the Co 2p_{1/2} region. Additionally, there are satellite peaks visible between the two notable peaks which originated from the shake-up process of electrons [49]. Apparently, the detection of the Co species is consistent with the XRD findings. With the introduction of Ni to the catalyst system, Co 2p_{3/2} and Co 2p_{1/2} peaks moved to higher BE with maximum peaks recorded around 792.3 eV (Co 2p_{3/2}) and 806.3 eV (Co 2p_{1/2}). The movement of Co 2p peaks to higher BE is indicative of a decrease in the electron density of the Co species, thus signifying the formation of Ni–Co in the bimetallic catalysts [34].

XPS spectra for Ni 2p species are represented in Fig. 9(c). The low binding energy peak can be assigned to Ni 2p_{3/2} (872.8–874.7 eV) and the high energy peak is ascribed to Ni 2p_{1/2} (878.7–880.9 eV) [50].

Table 6
Comparison of performance of selected promoted catalysts with the same operating conditions.

Catalysts	Operating Parameter			Catalytic performance				Ref
	T(K)	Feed ratio	GHSV (L g _{cat} ⁻¹ h ⁻¹)	Glycerol conversion (%)	H ₂ Yield (%)	CO Yield (%)	H ₂ /CO ratio	
5%Re-15%Ni/CaO	973	1	36	54.2	48.5	–	–	[18]
3%Re-15%Ni/SBA-15	973	1	36	57.0	51.0	–	–	[45]
3%Ag-15%Ni/Al ₂ O ₃	973	1	36	33.4	26.0	80.0	0.44	[19]
3%Ni-12%Co/Al ₂ O ₃	973	1	72	71.8	62.5	43.6	1.43	This work

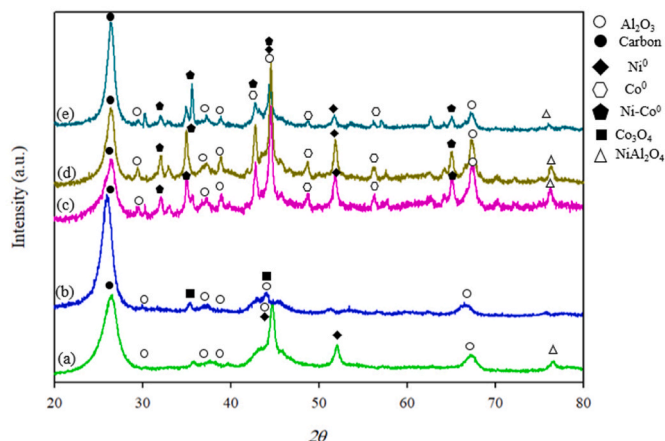


Fig. 8. XRD analyses of spent catalysts including (a) 15%Ni/Al₂O₃, (b) 15%Co/Al₂O₃, (c) 3%Ni-12%Co/Al₂O₃, (c) 7.5%Ni-7.5%Co/Al₂O₃ and (d) 10.5%Ni-4.5%Co/Al₂O₃ after GDR at T = 1073 K and F_{CO₂} : F_{C₃H₈O₃} = 1 : 1

Based on the deconvolution peaks, At Ni 2p_{3/2} region, two prominent peaks were detected (representing Ni²⁺ and NiAl₂O₄) located around 856.6–862.7 eV (Ni/Al₂O₃), 856.0–862.1 (3%Ni-12%Co/Al₂O₃), 856.3–862.3 (7.5%Ni-7.5%Co/Al₂O₃) and 856.4–862.6 (0.5%Ni-4.5%Co/Al₂O₃). Also, two deconvoluted peaks at higher Ni 2p_{1/2} were also detected in the range 878.7–880.9 eV belonging to metallic Ni⁰ and NiAl₂O₄, respectively [51]. As observed in the Co 2p spectra, a peak shift is also seen in the Ni species. The introduction of Co into Ni causes Ni 2p peaks to shift to lower BE. The changes of the Ni peaks to lower BE and Co to higher BE in the bimetallic catalysts compared to its mono-metallic counterpart suggests there is a strong electronic interaction between the bi-metals species thereby forming Ni-Co bimetallic alloys. In the course of the electronic interaction, there is electron transfer from Co to Ni which results in higher BE of Co 2p_{3/2} in the bimetallic catalyst [30]. More also, the electron density transfer from Co to Ni contributes to the catalyst's ability to maintain its performance. Hence, carbon deposition on the metal surface was reduced with increased oxidation leading to further improvement in the catalytic activity [52].

In addition, the atomic ratios of Ni/Al₂O₃, Co/Al₂O₃ and Ni-Co/Al₂O₃ were evaluated to reveal the effect of the bimetallic components on the dispersion of metal over Al₂O₃ support. The increase in atomic ratio was in the following order; 15%Ni/Al₂O₃ (0.15%) < 15%Co/Al₂O₃ (0.18%) < 10.5%Ni-4.5%Co/Al₂O₃ (1.76%) < 7.5%Ni-7.5%Co/Al₂O₃ (1.83%) < 3%Ni-12%Co/Al₂O₃ (2.25%). This trend corresponds to the improved dispersion of the Ni-Co bimetallic catalyst when compared to its mono-metallic counterpart. Bachiller-Baeza et al. also observed an improvement in the atomic ratio of the bimetallic catalysts, proving that bimetallic catalyst has a favorable impact on metal particle size [53]. 3% Ni-12%Co/Al₂O₃ exhibited the highest atomic ratio, consistent with the catalyst's smaller particle size and stronger metal-support interaction. This observation aligns with BET and H₂-TPR analysis, which demonstrated superiority in the catalytic performance compared to the other catalysts.

O 1s bands for spent catalysts are described in Fig. 9(d). Peak O_L and O_A were achieved by fitting into two Gaussian peaks at around

530.1–530.7 eV and 532.1–532.6 eV. The smaller peak (Peak O_L) described the surface lattice oxygen, while the larger peak (Peak O_A) was related to adsorbed surface oxygen [54]. The amount of oxygen vacancies can be estimated from the percentage of adsorbed oxygen, C_{oxy} (refer to Eq. (16)) that originated from oxygen vacancies that trapped the carbonate species existing on the catalysts' surface.

$$C_{oxy}(\%) = \frac{A_{O_A}}{A_{O_A} + A_{O_L}} \times 100\% \quad (16)$$

where A_{O_L} and A_{O_A} are integrated peak O_L and O_A, respectively.

The amount of oxygen vacancies for spent catalysts is listed as follows; 15%Ni/Al₂O₃ (25.1%) < 15%Co/Al₂O₃ (25.5%) < 10.5%Ni-4.5%Co/Al₂O₃ (64.4%) < 7.5%Ni-7.5%Co/Al₂O₃ (70.7%) < 3%Ni-12%Co/Al₂O₃ (75.2%). Also, increased oxygen vacancies on the catalyst surface could result in more active sites for CO₂ adsorption, which would help to mitigate carbon formation on the catalyst surface. The 3%Ni-12%Co/Al₂O₃ catalyst had the highest oxygen vacancies further clarifying the high catalytic performance and reduced carbon formation during the GDR reaction. Literature revealed that Ni-Co bi-metal catalyst possess O species resulting from Co oxygen affinity which aids removal of carbon and increases catalysts and process stability [40]. Also, for all bimetallic catalysts, Al 2p and O 1s peaks are similar further explaining the electron transfer between the bi-metals in the reduction process [55], in line with the H₂-TPR analysis.

Fig. 9(e) presents the extended C 1s spectra with all samples possessing two peaks. Peak C_I located at low binding energy detected at 284.6 eV, is assigned to graphite carbon which is sp²-bonded (C=C), whereas the peak C_{II} located around 285.3 eV is ascribed to amorphous carbon (C-C) sp³-bonded [56,57]. The 3%Ni-12%Co/Al₂O₃ catalyst recorded the lowest carbon formation which was consistent with the amount of oxygen vacancies recorded for each catalyst. The carbon suppression of the bimetallic catalysts could be attributed to its small crystallite size, high oxygen vacancies and strong basic characteristics [11]. For the crystallite size analysis, there is a direct relationship between the carbon formation rate and the catalysts' crystallite size [58, 59]. This is consistent with the order of crystallite size reported in the XRD analysis of the fresh catalysts. Moreover, high adsorbed CO₂ also contributed to the catalyst's high carbon resistivity since the CO₂ oxidized carbon species on the catalyst surface. The bimetallic catalysts had higher reactive filamentous carbon compared to Ni/Al₂O₃ and Co/Al₂O₃ (refer to Fig. 9(e)). The formation of filamentous carbon is more favorable compared to graphitic carbon because filamentous carbon is more reactive and easier to remove through oxidation processes. This is in direct contrast to graphitic carbon that can block the catalysts active sites and reduce catalytic activity [5,59].

3.7.3. Temperature-programmed oxidation (TPO)

TPO revealed the derivative weight loss and weight loss representations for the spent catalysts (refer to Fig. 10 and Fig. 11). Referring to Fig. 10, two obvious peaks; peak 1 (P1) at 400–600 K and peak 2 (P2) at < 600 K are seen for all the spent catalysts. According to literature, peaks in this region indicates carbon oxidation [60]. P1 represents the non-crystalline reactive amorphous carbon oxidation, while P2 is the less reactive graphitic carbon [61]. The formation of both amorphous and graphitic carbon via TPO was also verified by XPS analysis.

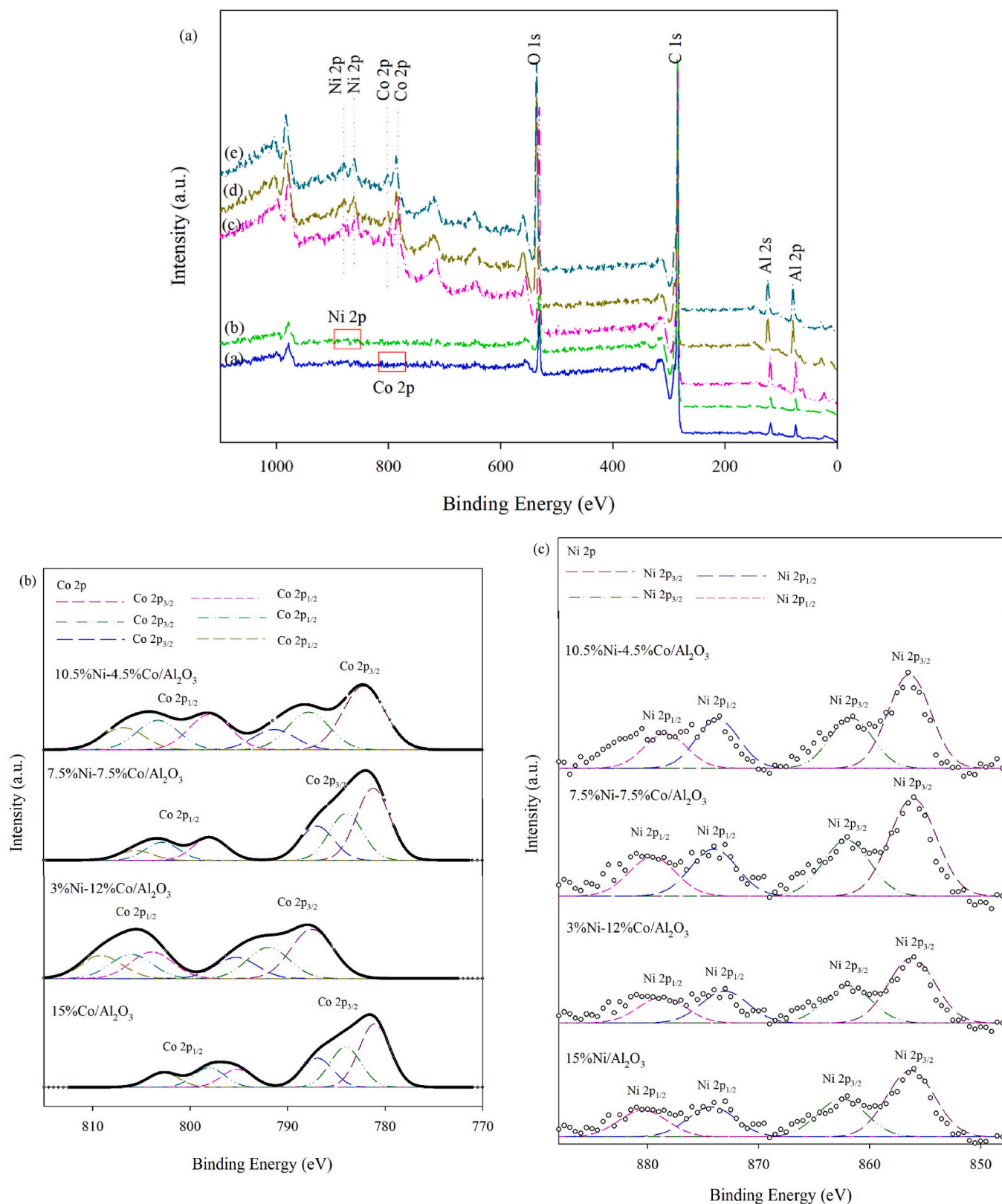


Fig. 9. (a) Overall XPS spectra, (b) Co 2p, (c) Ni 2p, (d) O 1s, (e) C 1s of spent catalysts after GDR at $T = 1073$ K and $F_{CO_2} : F_{C_3H_8O_3} = 1 : 1$

According to the reaction mechanism of this study, the carbon deposition on the catalyst's surface accumulated during glycerol decomposition and methane cracking. Nevertheless, the graphite peak intensity in the bimetallic catalysts significantly lessened, which is consistent with

the XRD evaluation previously discussed.

Also, the percentage weight loss declined in the order of 15%Ni/Al₂O₃ (34.27%) > 15%Co/Al₂O₃ (32.66%) > 12%Ni–3%Co/Al₂O₃ (27.71%) > 10.5%Ni-4.5%Co/Al₂O₃ (25.59%) > 7.5%Ni-7.5%Co/

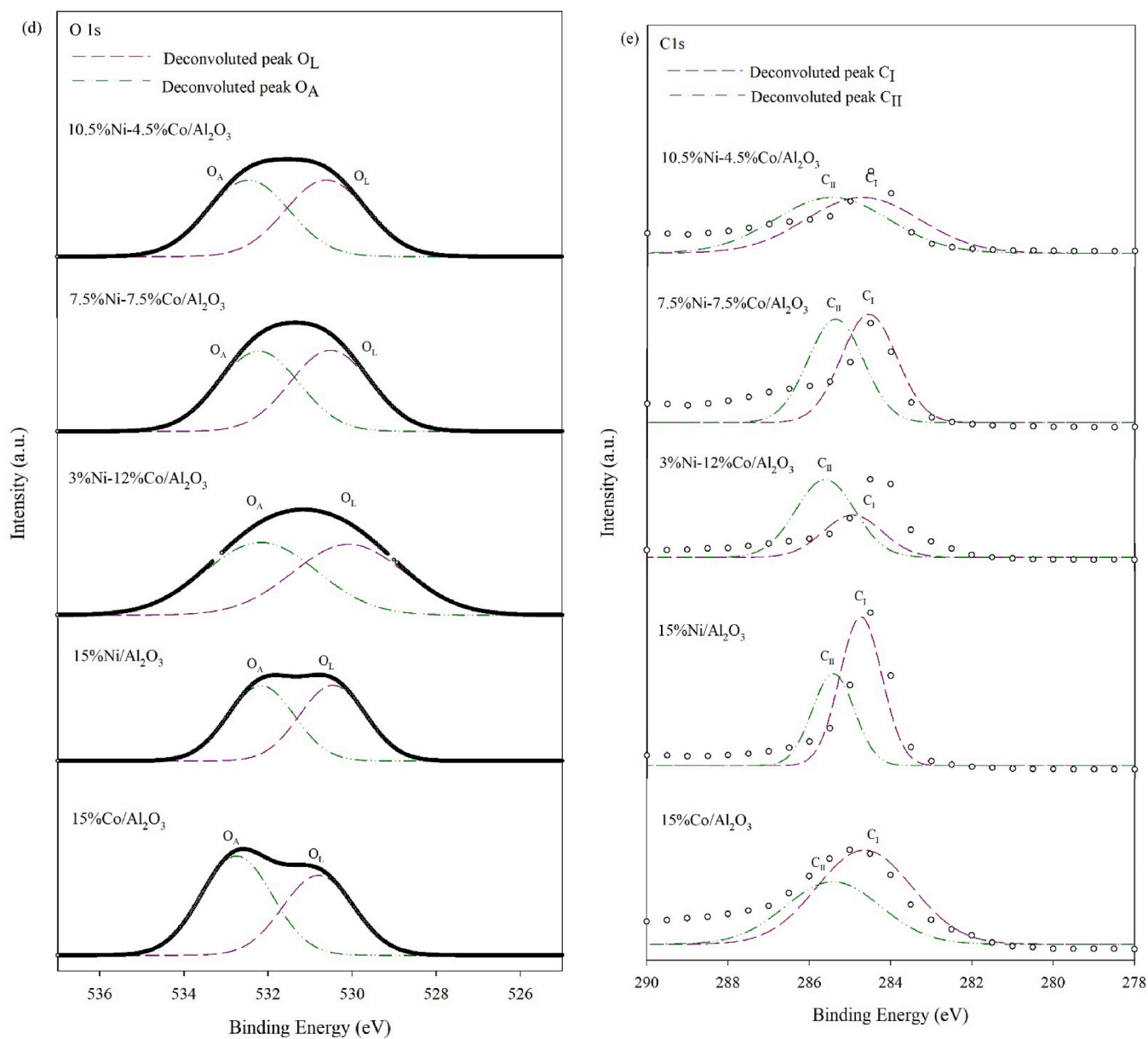


Fig. 9. (continued).

Table 7
Summary of binding energies for XPS peaks of mono- and bimetallic Ni–Co catalysts.

XPS Spectra	Binding energy (eV)					Peaks	Ref.
	15%Co/Al ₂ O ₃	15%Ni/Al ₂ O ₃	3%Ni–12%Co/Al ₂ O ₃	7.5%Ni–7.5%Co/Al ₂ O ₃	10.5%Ni–4.5%Co/Al ₂ O ₃		
Al 2p	77.8	77.5	78.6	78.3	78.1	Al ₂ O ₃	[53]
Ni 2p _{3/2}	–	856.6	856.0	856.3	856.4	Ni ²⁺	[39,75]
	–	862.7	862.1	862.3	862.6	NiAl ₂ O ₄	
Ni 2p _{1/2}	–	874.7	872.8	873.4	873.7	Ni ⁰	[33,45]
	–	880.9	878.7	879.6	879.8	NiAl ₂ O ₄	
Co 2p _{3/2}	780.5	–	787.6	781.7	782.1	Co ₃ O ₄	[33,45]
	783.8	–	792.3	784.1	787.8		
	787.2	–	795.3	788.2	791.9		
	792.3	–	804.2	798.1	797.3		
Co 2p _{1/2}	797.9	–	806.3	802.8	803.4	Co ⁰	
	802.7	–	808.2	805.9	806.9		
C 1s	285.4	285.3	285.5	285.3	285.5	Amorphous carbon	[71,72]
	284.6	284.6	284.6	284.6	284.6	Graphitic carbon	
O 1s	532.6	532.1	532.2	532.1	532.5	Surface adsorbed oxygen	[69]
	530.7	530.4	530.1	530.4	530.5	Co ₃ O ₄ /NiAl ₂ O ₄ and/or Al ₂ O ₃	

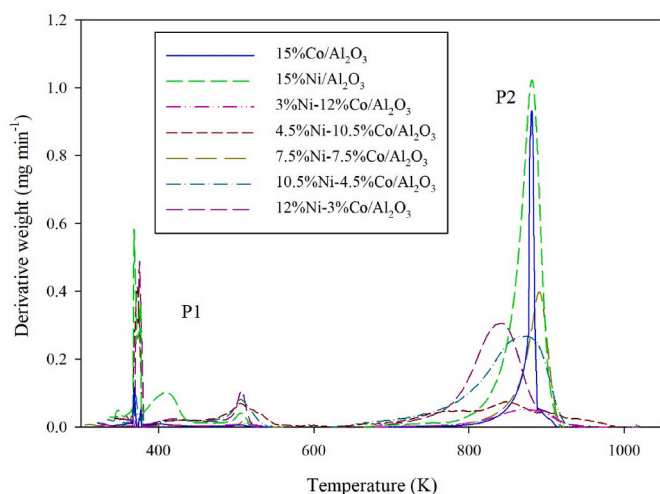


Fig. 10. TPO profiles of spent catalysts post GDR at $T = 1073$ K and $F_{CO_2} : F_{C_3H_8O_3} = 1 : 1$

Al_2O_3 (23.46%) > 4.5%Ni-10.5%Co/ Al_2O_3 (21.88%) > 3%Ni-12%Co/ Al_2O_3 (18.12%) (see Table S2 in the Supplementary Data). The reduction of carbon confirmed the effectiveness of the coke resistance bimetallic catalysts because of its high oxygen vacancies and strong basic characteristics. The high CO_2 adsorbed by the bimetallic catalysts enhanced the basicity of the catalysts. As a result, the adsorbed CO_2 by the catalysts aided the oxidation of carbon species [62]. Hence, the reduction of carbon formed when the 3%Ni-12%Co/ Al_2O_3 catalyst was employed compared to catalyst with different loading.

3.7.4. Transmission electron microscopy (TEM)

Fig. 12 shows the TEM images of spent samples after 8 h of reaction at 1073 K using 15%Ni/ Al_2O_3 , 15%Co/ Al_2O_3 and 3%Ni-12%Co/ Al_2O_3 catalyst. Ni and Co particles are the dark dots incorporated on Al_2O_3 support. Some agglomerations are detected on the mono-metallic catalysts, making the size of Ni and Co bigger (refer to Fig. 12(a) and (b)). The changes in metal particle size are as follows; 15%Ni/ Al_2O_3 (12.63

nm-13.49 nm), 15%Co/ Al_2O_3 (12.55 nm-13.37 nm) and 3%Ni-12%Co/ Al_2O_3 (9.25 nm-8.66 nm). The reduction in particles size for the Ni-Co bimetallic catalysts is due to visibly less agglomeration, suggesting that Ni-Co alloy improved metal distribution over the Al_2O_3 support. The 3% Ni-12%Co catalyst had the smallest crystallite size. Thus, 3%Ni-12%Co catalyst exhibited improved sintering resistibility compared to the mono-metallic catalyst. Graphite and carbon nano-filaments (CNF) were clearly visible in all spent catalysts. This observation was in agreement with both XPS and TPO analyses. CNF carbon has less impact on catalytic activity since it can easily be oxidized from the catalyst surface when compared to graphitic carbon [63]. CNF can be removed through gasification with CO_2 thereby allowing accessibility of reactants to the catalyst's active metal site [64]. For the graphitic carbon, it interrupts the accessibility of reactants to the active site by encapsulating the surface of the active metal.

Due to glycerol and methane decomposition at high reaction temperature carbon formation is unavoidable during the GDR reaction, however, carbon deposition was significantly reduced with the use of the bimetallic catalysts (refer to Fig. 12). This observation is in line with the previous discussion related to the XRD, XPS and TPO characterizations. The formation of graphitic and CNF has also been reported in other studies using different types of catalysts such as promoted Re-Ni/ CaO [18], Ag-Ni/ Al_2O_3 [19] and La-Ni/ Al_2O_3 [65].

4. Conclusions

The effect of Ni-Co/ Al_2O_3 bimetallic catalyst with respect to the physicochemical properties and catalytic activity on the GDR reaction was examined by varying reaction temperature. Mono-metallic (15%Ni/ Al_2O_3 and 15%Co/ Al_2O_3) and bimetallic Ni-Co/ Al_2O_3 catalysts with various loading were prepared by employing the ultrasonic-assisted impregnation method.

From the characterization studies, metal crystallite size reduced from 12.63 nm to 9.25 nm with the introduction of bimetallic Ni-Co which is linked to the diluting effect of the bimetallic precursors and enhanced metal dispersion of the catalyst. The increasing consumption of H_2 uptake during H_2 -TPR indicates that metal-support interaction was more prominent in the bimetallic samples. A similar trend was notable in CO_2 -

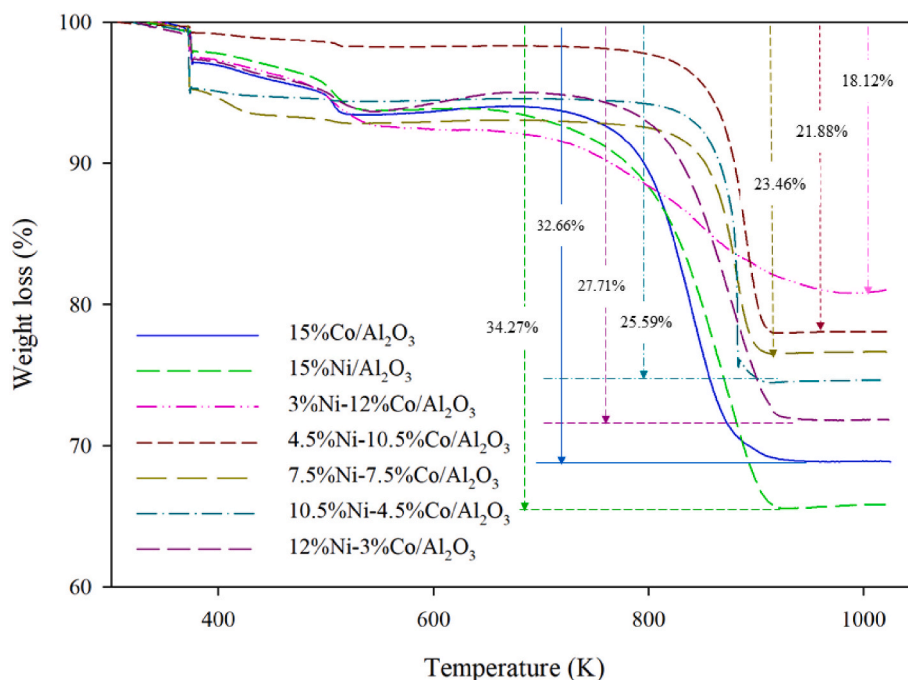


Fig. 11. Weight loss from TPO studies of the spent catalysts post GDR at $T = 1073$ K and $F_{CO_2} : F_{C_3H_8O_3} = 1 : 1$

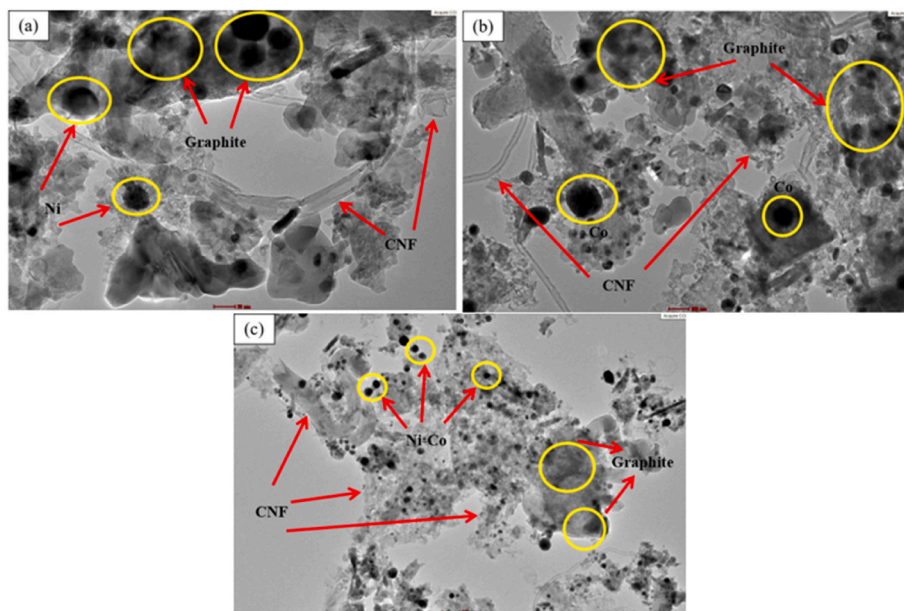


Fig. 12. TEM micrographs of the spent (a) 15%Ni/Al₂O₃, (b) 15%Co/Al₂O₃ and (c) 3%Ni–12%Co/Al₂O₃ after GDR at T = 1073 K and $F_{CO_2} : F_{C_3H_8O_3} = 1 : 1$

TPD analysis in which the Ni–Co bimetallic catalyst acquired more CO₂ uptake than its mono-metallic counterpart. FESEM-EDX analysis also indicated that the dispersion and distribution of the Ni and Co particles were extensive on the Al₂O₃ support.

According to the results, the catalytic performance followed the order; 3%Ni–12%Co/Al₂O₃ > 4.5%Ni–10.5%Co/Al₂O₃ > 7.5%Ni–7.5%Co/Al₂O₃ > 10.5%Ni–4.5%Co/Al₂O₃ > 15%Co/Al₂O₃ > 15%Ni/Al₂O₃. 3%Ni–12%Co/Al₂O₃ bimetallic catalyst exhibited the best catalytic performance with 75.6% of glycerol converted, 64.7% of H₂ and 44.8% of CO yield, respectively. The Co⁰ also maintained its active phase throughout the reaction even in oxidizing condition due to the synergistic Ni–Co metal interaction as reported in the XRD analysis of the spent catalysts. Although, carbon was formed on all spent catalysts, the Ni–Co bimetallic catalysts reduced the amount of total carbon formed by exhibiting high oxygen vacancies and strong basic attributes. According to the TEM analysis, Ni–Co alloy particles achieved less agglomeration compared to its mono-metallic counterpart, suggesting that Ni–Co alloy improved the metal-metal dispersion on catalyst support.

In summary, 3%Ni–12%Co/Al₂O₃ achieved excellent GDR catalytic performance attributed to its small crystallite size, high oxygen vacancies and strong basic nature compared to other catalysts utilized in this study.

Declaration of competing interest

The authors declare that they have no known competing financial interests or personal relationships that could have appeared to influence the work reported in this paper.

Acknowledgements

The authors would like to acknowledge financial assistance from the Ministry of Higher Education, Malaysia through the Fundamental Research Grant Scheme - FRGS/1/2018/TK02/UMP/02/12 (RDU190197) and Universiti Malaysia Pahang (RDU1803118 and PGRS200361) for financial support. The Doctoral Research Scheme (DRS) scholarship awarded to Ms. Shafiqah by the Universiti Malaysia Pahang is greatly appreciated.

Appendix A. Supplementary data

Supplementary data to this article can be found online at <https://doi.org/10.1016/j.joei.2022.09.008>.

References

- [1] S. Singh, M.B. Bahari, B. Abdullah, P.T.T. Phuong, Q.D. Truong, D.V.N. Vo, A. A. Adesina, Bi-reforming of methane on Ni/SBA-15 catalyst for syngas production: influence of feed composition, *Int. J. Hydrogen Energy* 43 (2018) 17230–17243, <https://doi.org/10.1016/j.ijhydene.2018.07.136>.
- [2] M.T. Azizan, A. Aqsha, M. Ameen, S.Z. Abidin, F. Sher, Catalytic Reforming of Oxygenated Hydrocarbons for the Hydrogen Production: an Outlook, *Biomass Conv. Bioref.*, 2020, <https://doi.org/10.1007/s13399-020-01081-6>.
- [3] S. Bac, Z. Say, Y. Kocak, K.E. Ercan, M. Harfouche, E. Ozensoy, A.K. Avci, Exceptionally active and stable catalysts for CO₂ reforming of glycerol to syngas, *Appl. Catal., B* 256 (2019), 117808, <https://doi.org/10.1016/j.apcatb.2019.117808>.
- [4] Z. Xie, B. Yan, J.H. Lee, Q. Wu, X. Li, B. Zhao, D. Su, L. Zhang, J.G. Chen, Effects of oxide supports on the CO₂ reforming of ethane over Pt–Ni bimetallic catalysts, *Appl. Catal., B* 245 (2019) 376–388, <https://doi.org/10.1016/j.apcatb.2018.12.070>.
- [5] T. Hou, S. Zhang, Y. Chen, D. Wang, W. Cai, Hydrogen production from ethanol reforming: catalysts and reaction mechanism, *Renew. Sustain. Energy Rev.* 44 (2015) 132–148, <https://doi.org/10.1016/j.rser.2014.12.023>.
- [6] S. Bepari, N.C. Pradhan, A.K. Dalai, Selective production of hydrogen by steam reforming of glycerol over Ni/Fly ash catalyst, *Catal. Today* 291 (2017) 36–46, <https://doi.org/10.1016/j.cattod.2017.01.015>.
- [7] N.A. Roslan, S.Z. Abidin, O.U.M.N.N. Shafiqah, S.Y. Chin, Y.H. Taufiq-Yap, Extracted γ -Al₂O₃ from aluminum dross as a catalyst support for glycerol dry reforming reaction, *Mater. Today Proc.* 42 (2021) 63–68, <https://doi.org/10.1016/j.matpr.2020.09.390>.
- [8] H.D. Demsash, K.V.K. Kondamudi, S. Upadhyayula, R. Mohan, Ruthenium doped nickel-alumina-ceria catalyst in glycerol steam reforming, *Fuel* 169 (2018) 150–156, <https://doi.org/10.1016/j.fuproc.2017.09.017>.
- [9] A. Zawadzki, J.D.A. Bellido, A.F. Lucrédio, E.M. Assaf, Dry reforming of ethanol over supported Ni catalysts prepared by impregnation with methanolic solution, *Fuel Process. Technol.* 128 (2014) 432–440, <https://doi.org/10.1016/j.fuproc.2014.08.006>.
- [10] S. De, J. Zhang, R. Luque, N. Yan, Ni-based bimetallic heterogeneous catalysts for energy and environmental applications, *Energy Environ. Sci.* 9 (2016) 3314–3347, <https://doi.org/10.1039/C6EE02002J>.
- [11] Z. Bian, S. Kawi, Highly carbon-resistant Ni–Co/SiO₂ catalysts derived from phyllosilicates for dry reforming of methane, *J. CO₂ Util.* 18 (2017) 345–352, <https://doi.org/10.1016/j.jcou.2016.12.014>.
- [12] Z. Bian, S. Das, M.H. Wai, P. Hongmanorom, S. Kawi, A Review on bimetallic nickel-based catalysts for CO₂ reforming of methane, *ChemPhysChem* 18 (2017) 3117–3134, <https://doi.org/10.1002/cphc.201700529>.
- [13] R. Wang, S. Liu, X. Li, Y. Zhang, C. Xie, S. Zhou, Y. Qiu, S. Luo, F. Jing, W. Chu, Glycerol steam reforming for hydrogen production over bimetallic MNI/CNTs

- (M=Co, Cu and Fe) catalysts, *Catal. Today* 355 (2020) 128–138, <https://doi.org/10.1016/j.cattod.2019.07.040>.
- [14] Y. Wang, M. Chen, Z. Yang, T. Liang, S. Liu, Z. Zhou, X. Li, Bimetallic Ni-M (M = Co, Cu and Zn) supported on attapulgite as catalysts for hydrogen production from glycerol steam reforming, *Appl. Catal., A* 550 (2017) 214–227, <https://doi.org/10.1016/j.apcata.2017.11.014>.
- [15] P.S. Bulutoglu, Z. Say, S. Bac, E. Ozensoy, A.K. Avci, Dry reforming of glycerol over Rh-based ceria and zirconia catalysts: new insights on catalyst activity and stability, *Appl. Catal., A* 564 (2018) 157–171, <https://doi.org/10.1016/j.apcata.2018.07.027>.
- [16] M. Tavanarad, F. Meshkani, M. Rezaei, Synthesis and application of noble metal nanocatalysts supported on MgAl₂O₄ in glycerol dry reforming reaction, *Catal. Lett.* 148 (2018) 164–172, <https://doi.org/10.1007/s10562-017-2221-3>.
- [17] K.W. Siew, H.C. Lee, J. Gimbin, S.Y. Chin, M.R. Khan, Y.H. Taufiq-Yap, C. K. Cheng, Syngas production from glycerol-dry(CO₂) reforming over La-promoted Ni/Al₂O₃ catalyst, *Renew. Energy* 74 (2015) 441–447, <https://doi.org/10.1016/j.renene.2014.08.048>.
- [18] N.N.M. Arif, S.Z. Abidin, O.U. Osazuwa, D.V.N. Vo, M.T. Azizan, Y.H. Taufiq Yap, Hydrogen production via CO₂ dry reforming of glycerol over Re-Ni/CaO catalysts, *Int. J. Hydrogen Energy* 44 (2019) 20857–20871, <https://doi.org/10.1016/j.ijhydene.2018.06.084>.
- [19] N. Harun, S.Z. Abidin, O.U. Osazuwa, Y.H. Taufiq Yap, M.T. Azizan, Hydrogen production from glycerol dry reforming over Ag-promoted Ni/Al₂O₃, *Int. J. Hydrogen Energy* 44 (2019) 213–225, <https://doi.org/10.1016/j.ijhydene.2018.03.093>.
- [20] N.A. Roslan, S.Z. Abidin, O.U. Osazuwa, S.Y. Chin, Y.H. Taufiq-Yap, H₂-rich syngas from glycerol dry reforming over Ni-based catalysts supported on alumina from aluminum dross, *Int. J. Hydrogen Energy* 46 (2021) 30959–30975, <https://doi.org/10.1016/j.ijhydene.2021.03.162>.
- [21] M. Tavanarad, M. Rezaei, F. Meshkani, Production of syngas via glycerol dry reforming on Ni catalysts supported on mesoporous nanocrystalline Al₂O₃, *J. CO₂ Util.* 24 (2018) 298–305, <https://doi.org/10.1016/j.jcou.2018.01.009>.
- [22] B. Erdogan, H. Arbag, N. Yasyerli, SBA-15 supported mesoporous Ni and Co catalysts with high coke resistance for dry reforming of methane, *Int. J. Hydrogen Energy* 43 (2018) 1396–1405, <https://doi.org/10.1016/j.ijhydene.2017.11.127>.
- [23] C.S. Smoljan, J.M. Crawford, M.A. Carreon, Mesoporous microspherical NiO catalysts for the deoxygenation of oleic acid, *Catal. Commun.* 143 (2020), 106046, <https://doi.org/10.1016/j.catcom.2020.106046>.
- [24] M. Muttakin, S. Mitra, K. Thu, K. Ito, B.B. Saha, Theoretical framework to evaluate minimum desorption temperature for IUPAC classified adsorption isotherms, *Int. J. Heat Mass Tran.* 122 (2018) 795–805, <https://doi.org/10.1016/j.ijheatmasstransfer.2018.01.107>.
- [25] M.B. Bahari, H.D. Setiabudi, T. Nishino, N. Ayas, D.V.N. Vo, Coke-resistant Y₂O₃-promoted cobalt supported on mesoporous alumina for enhanced hydrogen production, *J. Energy Inst.* 94 (2021) 272–284, <https://doi.org/10.1016/j.joei.2020.09.011>.
- [26] A.H. Fakeeha, W.U. Khan, A.S. Al-Fatesh, A.E. Abasaed, M.A. Naem, Production of hydrogen and carbon nanofibers from methane over Ni-Co/Al catalysts, *Int. J. Hydrogen Energy* 40 (2018) 1774–1781, <https://doi.org/10.1016/j.ijhydene.2014.12.011>.
- [27] D. Raikwar, S. Majumdar, D. Shee, Synergistic effect of Ni-Co alloying on hydrodeoxygenation of guaiacol over Ni-Co/Al₂O₃ catalysts, *Mol. Catal.* 499 (2018), 111290, <https://doi.org/10.1016/j.mcat.2020.111290>.
- [28] A.G. Dachenkoy, O.V. Ischenko, O.V. Goncharuk, M.V. Borysenko, O. V. Mischanckuk, V.M. Gun'ko, D. Sternik, V.V. Lisnyak, Preparation and characterization of Ni-Co/SiO₂ nanocomposite catalysts for CO₂ methanation, *Appl. Nanosci.* 12 (2022) 349–359, <https://doi.org/10.1007/s13204-020-01650-1>.
- [29] M. Rahmati, B. Huang, M.K. Mortensen, K. Keyvanloo, T.H. Fletcher, B. F. Woodfield, W.C. Hecker, M.D. Argyle, Effect of different alumina supports on performance of cobalt Fischer-Tropsch catalysts, *J. Catal.* 359 (2018) 92–100, <https://doi.org/10.1016/j.jcat.2017.12.022>.
- [30] J. Horlyck, C. Lawrey, E.C. Lovell, R. Amal, J. Scott, Elucidating the impact of Ni and Co loading on the selectivity of bimetallic NiCo catalysts for dry reforming of methane, *Chem. Eng. J.* 352 (2018) 572–580, <https://doi.org/10.1016/j.cej.2018.07.009>.
- [31] D. Li, L. Zeng, X. Li, X. Wang, H. Ma, S. Assabumrungrat, J. Gong, Ceria-promoted Ni/SBA-15 catalysts for ethanol steam reforming with enhanced activity and resistance to deactivation, *Appl. Catal., B* 176–177 (2015) 532–541, <https://doi.org/10.1016/j.apcatb.2015.04.020>.
- [32] T.J. Siang, T.L.M. Pham, N.V. Cuong, P.T.T. Phuong, N.H.H. Phuc, Q.D. Truong, D. V.N. Vo, Combined steam and CO₂ reforming of methane for syngas production over carbon-resistant boron-promoted Ni/SBA-15 catalysts, *Micropor. Micropor. Mat.* 262 (2018) 122–132, <https://doi.org/10.1016/j.micromeso.2017.11.028>.
- [33] H. Ay, D. Üner, Dry reforming of methane over CeO₂ supported Ni, Co and Ni-Co catalysts, *Appl. Catal., B* 179 (2015) 128–138, <https://doi.org/10.1016/j.apcatb.2015.05.013>.
- [34] M. Kondeboina, S.S. Enumula, K.S. Reddy, P. Challa, D.R. Burri, S.R.R. Kamaraju, Bimetallic Ni-Co/γ-Al₂O₃ catalyst for vapour phase production of γ-valerolactone: deactivation studies and feedstock selection, *Fuel* 285 (2021), 119094, <https://doi.org/10.1016/j.fuel.2020.119094>.
- [35] J. Xiang, X. Wen, F. Zhang, Supported nickel-cobalt bimetallic catalysts derived from layered double hydroxide precursors for selective hydrogenation of pyrolysis gasoline, *Ind. Eng. Chem. Res.* 53 (2014) 15600–15610, <https://doi.org/10.1021/ie502721p>.
- [36] A. Rodriguez-gomez, A. Caballero, Bimetallic Ni-Co/SBA-15 catalysts for reforming of ethanol: how cobalt modifies the nickel metal phase and product distribution, *Mol. Catal.* 499 (2018) 122–130, <https://doi.org/10.1016/j.mcat.2018.02.011>.
- [37] P.K. Sharma, N. Saxena, A. Bhatt, C. Rajagopal, P.K. Roy, Synthesis of mesoporous bimetallic Ni-Cu catalysts supported over ZrO₂ by homogenous urea coprecipitation method for catalytic steam reforming of ethanol, *Catal. Sci. Technol.* 3 (2013) 1017–1026, <https://doi.org/10.1039/C2CY20563G>.
- [38] S. He, S. He, L. Zhang, X. Li, J. Wang, D. He, J. Lu, Y. Luo, Hydrogen production by ethanol steam reforming over Ni/SBA-15 mesoporous catalysts: effect of Au addition, *Catal. Today* 258 (2015) 162–168, <https://doi.org/10.1016/j.cattod.2015.04.031>.
- [39] M.N.N. Shahirah, J. Gimbin, S.S. Lam, Y.H. Ng, C.K. Cheng, Synthesis and characterization of a La-Ni/α-Al₂O₃ catalyst and its use in pyrolysis of glycerol to syngas, *Renew. Energy* 132 (2019) 1389–1401, <https://doi.org/10.1016/j.renene.2018.09.033>.
- [40] Y. Turap, T. Wang, T. Fu, Y. Wu, Y. Wang, W. Wang, Co-Ni alloy supported on CeO₂ as a bimetallic catalyst for dry reforming of methane, *Int. J. Hydrogen Energy* 45 (2020) 6538–6548, <https://doi.org/10.1016/j.ijhydene.2019.12.223>.
- [41] V.S. Gharahshiran, M. Yousefpour, Synthesis and characterization of Zr-promoted Ni-Co bimetallic catalyst supported OMC and investigation of its catalytic performance in steam reforming of ethanol, *Int. J. Hydrogen Energy* 43 (2020) 7020–7037, <https://doi.org/10.1016/j.ijhydene.2018.02.139>.
- [42] A. Dehghanpoor-Gharashah, M. Rezaei, F. Meshkani, Preparation and improvement of the mesoporous nanostructured nickel catalysts supported on magnesium aluminate for syngas production by glycerol dry reforming, *Int. J. Hydrogen Energy* 46 (2021) 22454–22462, <https://doi.org/10.1016/j.ijhydene.2021.04.072>.
- [43] X. Wang, M. Li, M. Wang, H. Wang, S. Li, S. Wang, X. Ma, Thermodynamic analysis of glycerol dry reforming for hydrogen and syngas production, *Fuel* 88 (2009) 148–2153, <https://doi.org/10.1016/j.fuel.2009.01.015>.
- [44] S. Nanda, R. Rana, Y. Zheng, J.A. Kozinski, A.K. Dalai, Insights on pathways for hydrogen generation from ethanol, *Sustain. Energy Fuels* 1 (2017) 1232–1245, <https://doi.org/10.1039/C7SE00212B>.
- [45] N.A. Roslan, N.N.M. Arif, J.L. Jaspin, N.A.M. Razali, S.Z. Abidin, Hydrogen production by glycerol dry reforming over rhenium promoted Ni-based catalyst supported on Santa Barbara Amorphous 15 (SBA-15), *Energy Sources, Part A Recovery, Util. Environ. Eff.* 44 (2019) 1495–1507, <https://doi.org/10.1080/15567036.2019.1645762>.
- [46] X. Zhang, Y. Junhui, Y. Jing, C. Ting, X. Bei, L. Zhe, Z. Kunfeng, Y. Ling, H. Dannong, Excellent low-temperature catalytic performance of nanosheet Co-Mn oxides for total benzene oxidation, *Appl. Catal., A* 566 (2018) 104–112, <https://doi.org/10.1016/j.apcata.2018.05.039>.
- [47] M. Chen, X. Li, Y. Wang, C. Wang, T. Liang, H. Zhang, Z. Yang, Z. Zhou, J. Wang, Hydrogen generation by steam reforming of tar model compounds using lanthanum modified Ni/sepiolite catalysts, *Energy Convers. Manag.* 184 (2019) 315–326, <https://doi.org/10.1016/j.enconman.2019.01.066>.
- [48] N. Rahemi, M. Haghighi, A.A. Babaluo, S. Allahyari, M.F. Jafari, Syngas production from reforming of greenhouse gases CH₄/CO₂ over Ni-Cu/Al₂O₃ nanocatalyst: impregnated vs. plasma-treated catalyst, *Energy Convers. Manag.* 84 (2014) 50–59, <https://doi.org/10.1016/j.enconman.2014.04.016>.
- [49] J. Choi, H. Oh, S. Han, S. Ahn, J. Noh, J.B. Park, Preparation and characterization of graphene oxide supported Cu, Cu₂O and CuO nanocomposites and their high photocatalytic activity for organic dye molecule, *Curr. Appl. Phys.* 17 (2017) 137–145, <https://doi.org/10.1016/j.cap.2016.11.020>.
- [50] L. Tan, C. Qin, Z. Zhang, J. Ran, V. Manovic, Compatibility of NiO/CuO in Ca-Cu Chemical Looping for High-Purity H₂ Production with CO₂ Capture Energy Technol., vol. 6, 2018, pp. 1777–1787, <https://doi.org/10.1002/ente.201700894>.
- [51] A. Horváth, M. Némethi, A. Beck, B. Maróti, G. Sáfrán, G. Pantaleo, L.F. Liotta, A. M. Venezia, V. La Parola, Strong impact of indium promoter on Ni/Al₂O₃ and Ni/CeO₂-Al₂O₃ catalysts used in dry reforming of methane, *Appl. Catal., A* 621 (2021), 118174, <https://doi.org/10.1016/j.apcata.2021.118174>.
- [52] X. Guo, H. Liu, B. Wang, Q. Wang, R. Zhang, Insight into C + O(OH) reaction for carbon elimination on different types of CoNi(111) surfaces: a DFT study, *RSC Adv.* 5 (2015) 19970–19982, <https://doi.org/10.1039/C4RA15555F>.
- [53] B. Bachiller-Baeza, A. Iglesias-Juez, G. Agostini, E. Castillejos-López, Pd-Au bimetallic catalysts supported on ZnO for selective 1,3-butadiene hydrogenation, *Catal. Sci. Technol.* 10 (2020) 2503–2512, <https://doi.org/10.1039/C9CY02395J>.
- [54] N. Wang, K. Shen, L. Huang, X. Yu, W. Qian, W. Chu, Acile route for synthesizing ordered mesoporous Ni-Ce-Al oxide materials and their catalytic performance for methane dry reforming to hydrogen and syngas, *ACS Catal.* 3 (2013) 1638–1651, <https://doi.org/10.1021/cs4003113>.
- [55] X. Huang, C. Ji, C. Wang, F. Xiao, N. Zhao, N. Sun, W. Wei, Y. Sun, Ordered mesoporous CoO-NiO-Al₂O₃ bimetallic catalysts with dual confinement effects for CO₂ reforming of CH₄, *Catal. Today* 281 (2017) 241–249, <https://doi.org/10.1016/j.cattod.2016.02.064>.
- [56] C.A. Campos-Roldán, G. Ramos-Sánchez, R.G. Gonzalez-Huerta, J.R. Vargas García, P.B. Balbuena, N. Alonso-Vante, Influence of sp-sp carbon nanodomains on metal/support interaction, catalyst durability, and catalytic activity for the oxygen reduction reaction, *ACS Appl. Mater. Interfaces* 8 (2016) 23260–23269, <https://doi.org/10.1021/acsami.6b06886>.
- [57] S. Xu, H. Zhu, W. Cao, Z. Wen, J. Wang, C.P. François-Xavier, T. Wintgens, Cu-Al₂O₃-g-C₃N₄ and Cu-Al₂O₃-C-dots with dual-reaction centres for simultaneous enhancement of Fenton-like catalytic activity and selective H₂O₂ conversion to hydroxyl radicals, *Appl. Catal., B* 234 (2018) 223–233, <https://doi.org/10.1016/j.apcatb.2018.04.029>.

- [58] T. Osaki, Effect of Nickel diameter on the rates of elementary steps involved in CO₂ reforming of CH₄ over Ni/Al₂O₃ catalysts, *Catal. Lett.* 145 (2015) 1931–1940, <https://doi.org/10.1007/s10562-015-1608-2>.
- [59] J. Xin, H. Cui, Z. Cheng, Z. Zhou, Bimetallic Ni-Co/SBA-15 catalysts prepared by urea co-precipitation for dry reforming of methane, *Appl. Catal., A* 554 (2018) 95–104, <https://doi.org/10.1016/j.apcata.2018.01.033>.
- [60] S. Isarapakdeetham, P. Kim-Lohsoontorn, S. Wongsakulphasatch, W. Kiatkittipong, N. Laosiripojana, J. Gong, S. Assabumrungrat, Hydrogen production via chemical looping steam reforming of ethanol by Ni-based oxygen carriers supported on CeO₂ and La₂O₃ promoted Al₂O₃, *Int. J. Hydrogen Energy* 45 (2019) 1477–1491, <https://doi.org/10.1016/j.ijhydene.2019.11.077>.
- [61] A. Larimi, F. Khorasheh, Renewable hydrogen production by ethylene glycol steam reforming over Al₂O₃ supported Ni-Pt bimetallic nano-catalysts, *Renew. Energy* 128 (2018) 188–199, <https://doi.org/10.1016/j.renene.2018.05.070>.
- [62] T. Nejat, P. Jalalinezhad, F. Hormozi, Z. Bahrami, Hydrogen production from steam reforming of ethanol over Ni-Co bimetallic catalysts and MCM-41 as support, *J. Taiwan Inst. Chem. Eng.* 97 (2019) 216–226, <https://doi.org/10.1016/j.jtice.2019.01.025>.
- [63] M.N. Younis, Z.O. Malaibari, W. Ahmad, S. Ahmed, Hydrogen production through steam reforming of diesel over highly efficient promoted Ni/γ-Al₂O₃ catalysts containing lanthanide series (La, Ce, Eu, Pr, and Gd) promoters, *Energy Fuel*. 32 (2018) 7054–7065, <https://doi.org/10.1021/acs.energyfuels.8b00890>.
- [64] P. Djinović, I.G.O. Črnivec, B. Erjavec, A. Pintar, Influence of active metal loading and oxygen mobility on coke-free dry reforming of Ni-Co bimetallic, *Appl. Catal., B* 125 (2012) 259–270, <https://doi.org/10.1016/j.apcatb.2012.05.049>.
- [65] K.W. Siew, H.C. Lee, M.R. Khan, J. Gim bun, C.K. Cheng, CO₂ reforming of glycerol over La-Ni/Al₂O₃ catalyst: a longevity evaluative study, *J. Energy Chem.* 24 (2015) 366–373, [https://doi.org/10.1016/S2095-4956\(15\)60324-2](https://doi.org/10.1016/S2095-4956(15)60324-2).